Biomaterials Advances 153 (2023) 213568

Contents lists available at ScienceDirect

Biomaterials Advances

journal homepage: www.journals.elsevier.com/materials-science-and-engineering-c

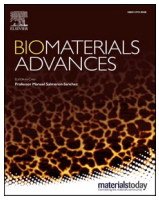

Transdermal wires for improved integration in vivo

Andreas P. Kourouklis [a], Julius Kaemmel [d], Xi Wu [a], Miguel Baños [a], Astrid Chanfon [c], Simone de Brot [c], Aldo Ferrari [b], Nikola Cesarovic [d,e], Volkmar Falk [d,e], Edoardo Mazza [a,b,*]

[a] Department of Mechanical and Process Engineering, Institute for Mechanical Systems, ETH Zurich, 8092 Zurich, Switzerland
[b] EMPA, Swiss Federal Laboratories for Material Science and Technology, 8600 Dübendorf, Switzerland
[c] COMPATH, Institute of Animal Pathology, University of Bern, 3012 Bern, Switzerland
[d] Department of Cardiothoracic and Vascular Surgery, German Heart Center Berlin, 13353 Berlin, Germany
[e] Department of Health Sciences and Technology, ETH Zürich, 8093 Zürich, Switzerland

ARTICLE INFO

Keywords:
VAD drivelines
In vivo
Geometry
Free-form topography
Epidermal downgrowth
Inflammation
Power transfer
Fibrosis
Driveline infection

ABSTRACT

Alternative engineering approaches have led the design of implants with controlled physical features to minimize adverse effects in biological tissues. Similar efforts have focused on optimizing the design features of percutaneous VAD drivelines with the aim to prevent infection, omitting however a thorough look on the implant-skin interactions that govern local tissue reactions. Here, we utilized an integrated approach for the biophysical modification of transdermal implants and their evaluation by chronic sheep implantation in comparison to the standard of care VAD drivelines. We developed a novel method for the transfer of breath topographical features on thin wires with modular size. We examined the impact of implant's diameter, surface topography, and chemistry on macroscopic, histological, and physical markers of inflammation, fibrosis, and mechanical adhesion. All implants demonstrated infection-free performance. The fibrotic response was enhanced by the increasing diameter of implants but not influenced by their surface properties. The implants of small diameter promoted mild inflammatory responses with improved mechanical adhesion and restricted epidermal downgrowth, in both silicone and polyurethane coated transdermal wires. On the contrary, the VAD drivelines with larger diameter triggered severe inflammatory reactions with frequent epidermal downgrowth. We validated these effects by quantifying the infiltration of macrophages and the level of vascularization in the fibrotic zone, highlighting the critical role of size reduction for the benign integration of transdermal implants with skin. This insight on how the biophysical properties of implants impact local tissue reactions could enable new solutions on the transdermal transmission of power, signal, and mass in a broad range of medical devices.

1. Introduction

The ultimate therapeutic treatment for patients with advanced heart failure (HF) is heart transplantation. Yet, the shortage of suitable organs and the rapidly precipitating patient health render the procedure unfit for many of them [1]. In this case, ventricular assist devices (VADs) offer a viable solution to heart transplantation for the repair of cardiac function. VAD comprises of a mechanical circulatory component which is connected to the heart tissue, and a central driveline that crosses the human skin to transport power and information signals from the battery and controller located outside the human body [2,3]. Owing the inherent risks of chronic transdermal implants, including infection and erosion, several efforts have been directed to developing fully implantable devices that could eliminate the need of percutaneous VAD drivelines. For the moment, major complications related to thermal injury, unreliable communication between remote components, and poor biocompatibility of the implanted equipment have slowed down the clinical adaptation of fully implantable VADs [4–8]. In this frame, percutaneous drivelines remain the most reliable and the only clinically approved method for power transport to VADs.

The long-term implantation of VAD drivelines however comes along with the serious risk of local pocket and driveline-specific infections (DLIs) (Fig. 1A), which can escalate to systemic infections [9–13]. DLIs are the most prevalent type of VAD infection throughout the duration of device implantation [14,15], accounting for ~30 % of adverse cases in the first 30 day of readmission [16]. Superficial DLIs manifest with

Abbreviations: VAD, Ventricular assist device; DLI, Driveline infection; HM-III, Heart Mate III.

* Corresponding author at: Department of Mechanical and Process Engineering, Institute for Mechanical Systems, Leonhardstrasse 21, 8092 Zürich, Switzerland.
E-mail address: mazza@imes.mavt.ethz.ch (E. Mazza).

https://doi.org/10.1016/j.bioadv.2023.213568
Received 8 February 2023; Received in revised form 13 July 2023; Accepted 23 July 2023
Available online 26 July 2023

symptoms of erythema, increased temperature, and purulent drainage at the exit site of the skin tissue, while deep DLIs bear signs of abscess into the lower layers of the soft tissue (e.g., muscle, fascia) [2,17]. DLIs result from the biofilm formation on VAD drivelines, typically due to bacteria harboring human epidermis [18–20].

Percutaneous implants (Fig. 1B) destruct the physiological barrier of the human skin in exchange of a poorly vascularized scar tissue that impedes immune competence [21,22], thus increasing the chance of infection [23–25]. Similar tissue effects burden the firm mechanical adhesion of implants to the skin, which is necessary for the prevention of epidermal downgrowth and biofilm invasion from the implant-skin interface to the subcutaneous tissue [26–29]. Several pre- and post-operation protocols have been developed against DLIs. These entail a combination of antibiotic prescriptions [30,31], wound treatment protocols [32,33], and driveline translocation or device exchange [34,35].

Because none of these strategies can fully resolve the problem and potentially the resurgence of DLIs, a different cohort of studies focused on the modification of physical and chemical properties of the drivelines that empirically correlate with the rise of DLI. Early clinical studies showed that more compliant and thin drivelines lower the occurrence of DLI [36], without however decoupling the effects of material chemistry in the compared drivelines. In addition, the porosity and surface topography of the drivelines have been suggested as factors that mediate integration with the skin tissue. For instance, the high surface porosity of mock drivelines facilitates skin ingrowth and enhances its adhesion with biological skin both in vivo and in vitro [37–40]. On the other hand, VAD drivelines with flat silicone surface appear less prone to infection than those of porous velour [41,42]. Although the surface modification of medical devices is a largely considered strategy for the mitigation of device-associated infections [43–45], the connection between surface topography and DLIs is less explored. The presentation of select topographical features on biomaterial surfaces is known to influence cell adhesion, yielding mild to moderate pro-fibrotic responses [46–50]. Harnessing a similar concept, VAD drivelines dressed with a protective layer of surface-engineered hydrogel were less exposed to bacterial colonization in vivo [51]. The direct transfer of topographical features on the curved driveline surface however imposes a technical challenge which is not easily addressed by conventional micropatterning [52,53].

Surface chemistry is yet another factor that can influence the integration of VAD drivelines with skin. For instance, silicone and velour materials promote stronger attachment of skin as compared to polyurethane [54]. Separate evidence showed that silicone drivelines delay DLIs by inhibiting abnormal skin growth, hyperkeratosis, and dermal inflammation, which on the contrary were enhanced by velour drivelines [55]. Similarly, the chemical composition of implanted sutures has been shown to influence the severity of tissue reactions and their stability in biological tissues [56,57], suggesting the critical role of surface chemistry for the biocompatibility of transdermal implants.

In spite of the presumed cause-effect relationship between VAD drivelines and DLIs, the local tissue effects that underline the foreign body reactions (FBRs) in response to the physical and chemical features of VAD drivelines remain poorly understood. This work examined the hypothesis that multiple transdermal wires producing a higher number of smaller individual wounds may improve skin integration as compared to the single, large wound produced by VAD drivelines. The tested configurations of transdermal wires displayed control over three independent parameters – their diameter, surface chemistry, and surface topography. Finally, the local tissue reactions and the mechanical adhesion of the transdermal wires were compared to Heart Mate III (HM-III) drivelines, pointing to the preferential use of implants with reduced diameter for improved integration with skin.

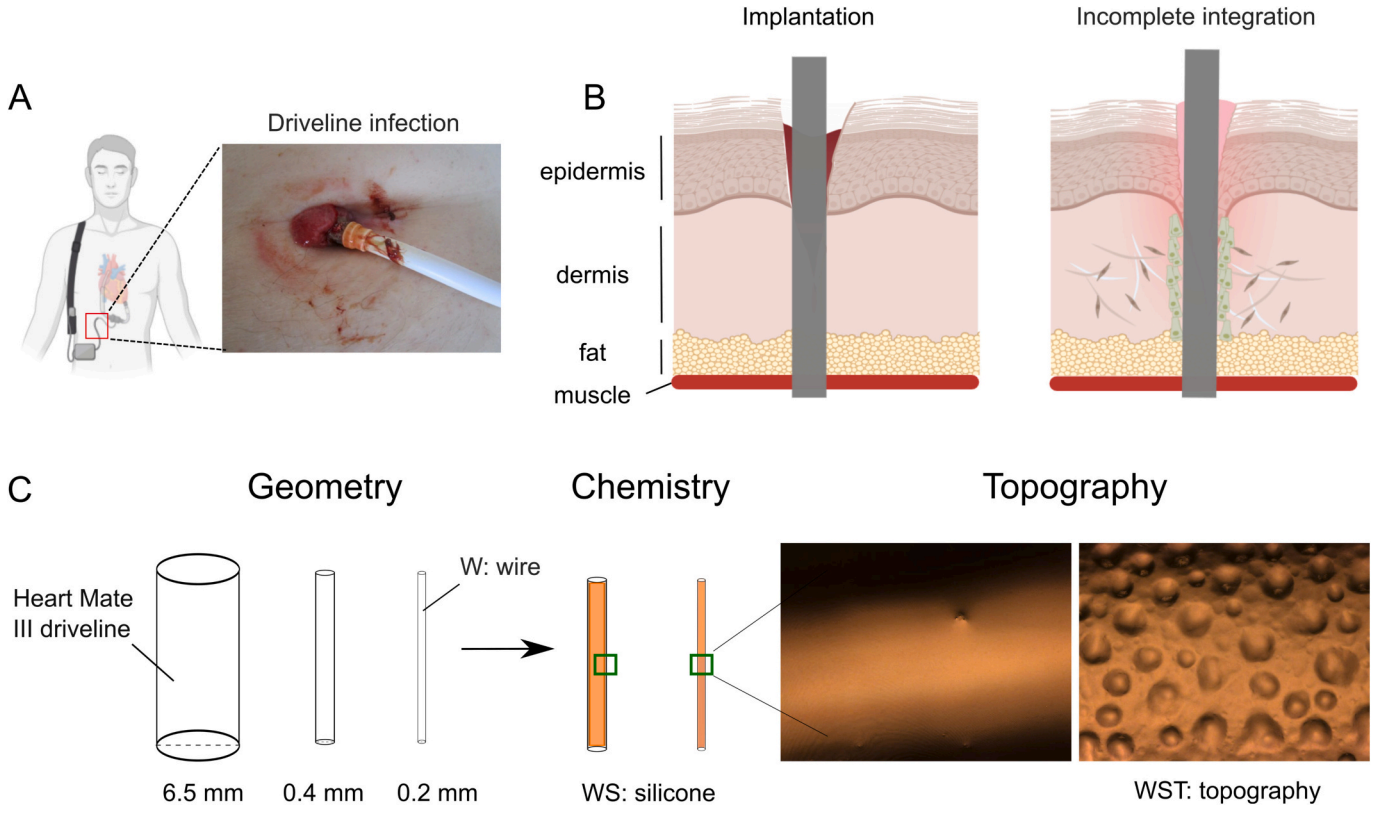

Fig. 1. Engineering transdermal wires with the potential to eliminate the problem of DLI. A) Deep DLI in patient with percutaneous VAD driveline. B) Percutaneous implants are poorly integrated with skin presumably due to adverse local tissue effects such as inflammation, epidermal downgrowth, and fibrosis. C) The design of conductive wires with tunable geometry, surface chemistry and surface topography defines a combinatorial strategy to develop new transdermal implants with improved biomechanical compatibility in order to protect the barrier function of the biological skin.

2. Results

2.1. Transdermal wire configurations with tunable biophysical features

Small size implants are generally better integrated with biological tissues [58]. This is also suggested by the positive effects of VAD drivelines with thin diameter against the progression of DLIs [36,59], establishing a strong incentive to develop new configurations of small drivelines. Here, the size of select wires was driven by previous evidence on wide sutures (e.g., 2/0 or D ~ 0.3 mm) which triggered relatively acute tissue reactions compared to thin sutures (4/0 or D ~ 0.15 mm), delaying this way the wound healing process and increasing the risk of infection [60].

Here, similarly thin wires (0.2 or 0.4 mm) were percutaneously implanted in an ovine animal model to investigate the effects of diameter, surface chemistry, and topography (Fig. 1C) on the efficiency of transdermal integration. The diameter of the select wires matches the size of the individual electrical cables in the commercial VAD drivelines [61,62]. The outer surface of enamel (polyurethane coated) wires (called "W") was further modified with biocompatible silicone (i.e., RTV) [2,63] under ambient conditions. The silicone-coated (called "WS") wires enabled the direct comparison with the HM-III drivelines (*Control*) which establish a silicone-skin interface (Fig. 1A) in the standard clinical treatment of VAD implantation [14,64,65]. Despite their known pro-fibrotic effects, silicones remain the most widespread choice for the surface functionalization of implantable devices [66].

Furthermore, we applied a novel method of free-form topography to obtain reproducible breath features with rationalized diameter (~35 ± 3 μm) and depth (~4 ± 0.4 μm) features (Fig. 1C) on the surface of silicone coated wires (called "WST") (Supplemental Fig. S1A & S1B). This topographical pattern of breath features was partially adapted to resemble texture profiles which were previously shown to enhance mechanical adhesion with the contacting tissue [37,67] and prevent fibrotic response [49,68,69]. In addition, substrates with similar breath features have been previously shown to protect the structure of endothelial monolayers against the destructive effects of shear stress [70]. Thus, the surface modification with breath features is likely to have a positive effect on the integration of transdermal implants.

2.2. Animal implantation and macroscopic observations of transdermal wires

A group of four adult female sheep (*Ovis aries*) was included in this study to obtain a complete description of the macroscopic symptoms caused by the implants on the wounded skin. Sheep represents a robust model of choice for testing new cardiovascular surgical protocols [71–73], because it enables the implementation of reproducible surgical portraits for chronic experiments of percutaneous skin implantation [74–76]. Sheep skin demonstrates an interlayer architecture [77], and it has been previously used to model the wound healing responses of the

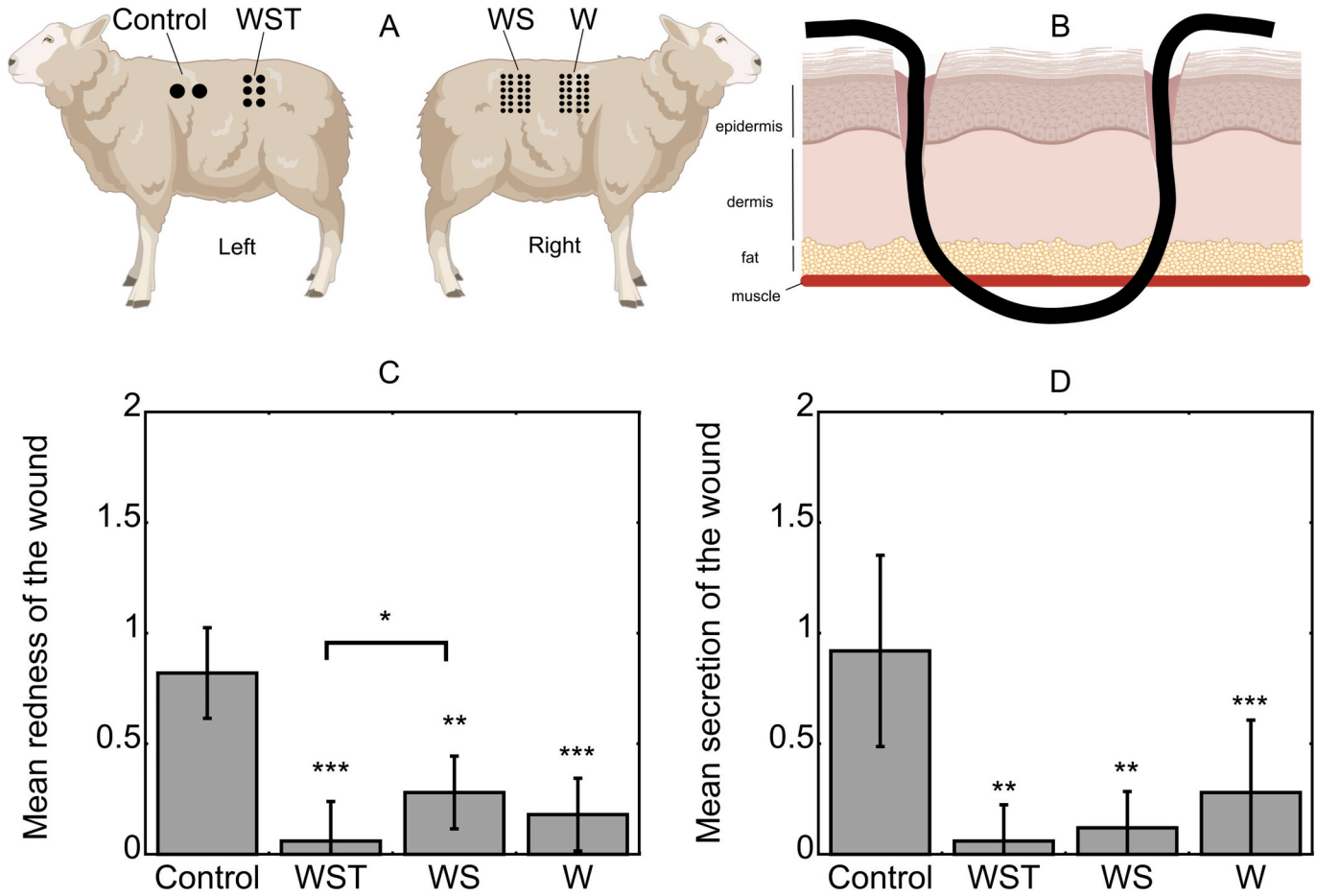

Fig. 2. In vivo evaluation of transdermal wires in a large animal model. A) An ovine model was used for the percutaneous implantation of the test wire configurations (W, WS, WST) and the *Control* implant. B) The surgical scheme presents one entry and one exit site to emulate the subcutaneous injury and the implant-skin interface associated with the clinical implantation of VAD drivelines. The symtoms of redness (C) and secretion (D) offer a representative macroscopic assessment of inflammation caused by the different implants on the skin tissue. Data present the mean ± s.e.m. from $n = 4$ animals observed at various time intervals in the first 2 weeks of the trial. *P*-values indicated for $P < 0.05$ (*), $P < 0.01$ (**), and $P < 0.001$ (***) relative to the *Control* implant. P-values for the pair comparison of the test wires (WST, WS, W) are indicated above the corresponding bars.

human skin [78,79]. In addition, sheep are docile and quiet [80], minimizing local tissue reactions related to the excessive mechanical movements of drivelines implanted in hyperactive animals such as minipigs [81,82].

Each animal of the study received four implants at equal surgical sites of their left and right flank (Fig. 2A), evenly distributed between their cranial and caudal sides. The test conditions were represented by three configurations with different numbers of wires to obtain equal conductive cross-sectional area with the 6 insulated metallic cables contained in the *Control* implants (conductive area: $A_{Control} \sim 0.76$ mm^2). Consequently, 3 WST, 12 WS ($D_{WS} \sim 0.2$ mm), and 12 W ($D_W \sim 0.2$ mm) wires were percutaneously implanted with a surgical scheme of one entrance and one exit per wire in the animal skin (Fig. 2B), matching this way the overall cross-sectional conductive area of 0.76 mm^2. It is noteworthy to point out that the outer diameter of the *Control* ($D_{Control} \sim 6.5$ mm) is significantly wider than that of WST ($D_{WST} \sim 0.5$ mm), WS ($D_{WS} \sim 0.26$ mm), and W ($D_W \sim 0.2$ mm) wires (Supplemental Fig.S1C), which imposes a large interface between the *Control* implant and the skin.

The animals were monitored for macroscopic symptoms of the wounds and sacrificed at 4 weeks after implantation. The period of the study is consistent with previous evidence on the rise of DLI diagnosis as early as ~4 weeks after implantation [13,16,83,84]. The clinical follow-up recorded a gain of body weight for all animals between implantation and termination without major abnormalities or visible sign of infection. Throughout the study, we recorded macroscopic symptoms which are regularly used for the preclinical and clinical evaluation of wound healing and infection, such as redness, secretion, heat, and swelling [85–87]. Semi-quantitative scoring revealed significant differences on redness and wound secretion (Fig. 2C & D), with the highest mean score registered for the *Control* condition. Neither swelling nor heat were noticed in any of the animals and implant conditions (Supplemental Table T2A-E). Similarly, no macroscopic signs of deep or superficial infection were detected for both the test and *Control* implants.

2.3. Local tissue reactions in response to the biophysical features of transdermal wires

Histopathological studies were led to identify morphological features that reflect the local tissue reactions around the transdermal wires (Fig. 3A). For this analysis, we adjusted previously established semi-quantitative scoring systems [24,88] to collectively evaluate the implant-associated tissue reactions regarding the presence of inflammatory cells, fibrotic area, and epidermal lining (Table 1). Based on that, the extent of fibrosis rather than the presence of leukocytes was more enhanced for the *Control* than the test wires (W, WS, WST). The score analysis shows that small wires induced minimal (both W and WS: 23.8 %) to mild (W: 38.1 % and WS: 57.1 %) reactions in most tissues (Fig. 3B). On the other hand, the larger implants triggered moderate to severe (WST: 69.2 % and *Control*: 81.8 %) inflammatory reactions for most tissues (Fig. 3B). This behavior was also mirrored in the average score of tissue reactivity for the different conditions – *Control*: 4.8 ± 0.4, WST: 4.3 ± 0.4, WS: 2.4 ± 0.6, and W: 2.7 ± 0.3 (mean ± standard error of the mean) (Supplemental Table T3A). Importantly, the histological studies found no evidence of inflammatory lesions that could be indicative of infection in any of the tested implant conditions.

2.4. Quantification of fibrotic responses in the dermal tissue

Fibrotic deposition is a characteristic process related to implant biocompatibility [89], and it is regularly evaluated by measuring the thickness or the area of the corresponding fibrous tissue [90,91]. Here, the *Control* implant displayed higher mean fibrotic area (~15mm^2 per tissue section) compared to the test implants (~1-3 mm^2 per tissue section), Fig. 4A. W and WST exhibited minimal fibrosis (<1mm^2) in one third of the analyzed tissues, while WS for most of the samples. The larger fibrotic area adjacent to the WST wires (2.9 ± 0.8 mm^2) compared to WS (0.9 ± 0.3 mm^2), reflects a pro-fibrotic effect of increasing implant diameter that prevails previously acknowledged anti-fibrotic signals of breath topography [46–49].

In a similar trend, the level of inflammation varied around small wires, with a percentage of W and WS samples devoid of infiltrated immune cells (Fig. 3B). A relevant feature of tissue reaction was additionally explored by quantifying the distribution of infiltrated macrophages in the fibrotic region through the expression of the characteristic protein marker iba-1 [92–94]. This analysis showed that the area occupied by iba-1 positive cells around the *Control* implant (~0.6 mm^2) was the largest among the tested implants (inset of Fig. 4A). Interestingly, the overall area occupied by iba-1 positive cells was larger for WST (~0.13 mm^2) than WS (~0.03 mm^2) and W (~0.02 mm^2) implants, establishing a positive correlation between macrophage presentation and the extent of fibrosis (Fig. 4A).

Another characteristic of wound healing connected to inflammation is that of vascularization [95–98]. Many lines of evidence show that vascularization plays a critical role for wound healing during implantation [99,100], and it can be responsive to biophysical cues such as implant topography [101,102]. For this reason, we performed immunostaining studies to quantify the CD-31 positive vascular vessels in the fibrotic zone. CD-31 is regularly used as a characteristic protein marker to quantify the angiogenic component of FBRs in subcutaneous implants [91,103–105]. We detected a ten-fold increase in the number of vascular vessels occupying the fibrotic tissue around the tunnel of the *Control* implant (~3000 vessels) compared to that of the test wires (WST: ~200, WS: ~250, W ~ 150 vessels) (Fig. 4B&E). In this case, vascularization positively correlates with the inflammatory signature of the *Control* but not the WST implants as depicted in Fig. 3B. In addition, no significant differences were deduced from the corresponding pair-comparison of the number of vascular vessels in the fibrotic zones of the test wires (i.e., WST, WS, and W). Beyond that, the vascular density (number of vessels/fibrotic area) and the average cross-sectional area of CD31 positive vessels (mm^2) in the fibrotic zone were similar for all implants (Supplemental Fig.F4A&B).

However, a closer look at the proximity of the implantation tunnels revealed the presence of an avascular zone with higher area for the *Control* implant (~2.8 mm^2) than the test wires (WST: ~0.3 mm^2, WS: ~0.1 mm^2, W: ~0.2 mm^2), Fig. 4C (Supplemental Fig.F4C). Similar to the overall fibrotic zone (Fig. 4A), the area of the avascular zone occupied by iba-1 positive cells is higher for the *Control* implant (~0.3 mm^2) than the test wires (WST: ~0.03 mm^2, WS: ~0.01 mm^2, W: ~0.01 mm^2), (inset of Fig. 4C). Interestingly, the avascular zone displayed higher density of iba-1 positive cells relative to the overall fibrotic zone (Supplemental Fig.F4D&E), indicating an accentuated fibrotic response close to the implants.

2.5. Characterization of the mechanical interactions at the skin-implant interface

Implant integration in biological tissues is regularly evaluated by the corresponding adhesion strength [90,106]. Stronger adhesion of transdermal implants shall impede friction with skin, limiting the repetitive actuation of inflammatory responses [107]. Here, the mechanical adhesion of the transdermal wires was assessed by measuring the force required for implant removal from the skin tissue (Fig. 5A&B) similar to previous protocols [108–111]. The shear stress, which is calculated by dividing the pull-off force for each implant with the corresponding interfacial area with skin, was approximately ten-fold lower for the *Control* implant (~0.013 ± 0.001 N/mm^2) than for the W (~0.14 ± 0.02 N/mm^2), WS (~0.1 ± 0.02 N/mm^2), and WST wires (~0.13 ± 0.03 N/mm^2), (Fig. 5C). No significant differences were found on the shear stress of decohesion between the W, WS, and WST wires. Since the number of wires composing each configuration (12 W, 12 WS, 3 WST) and the surgical scheme (1 entry and 1 exit site per wire) were chosen to

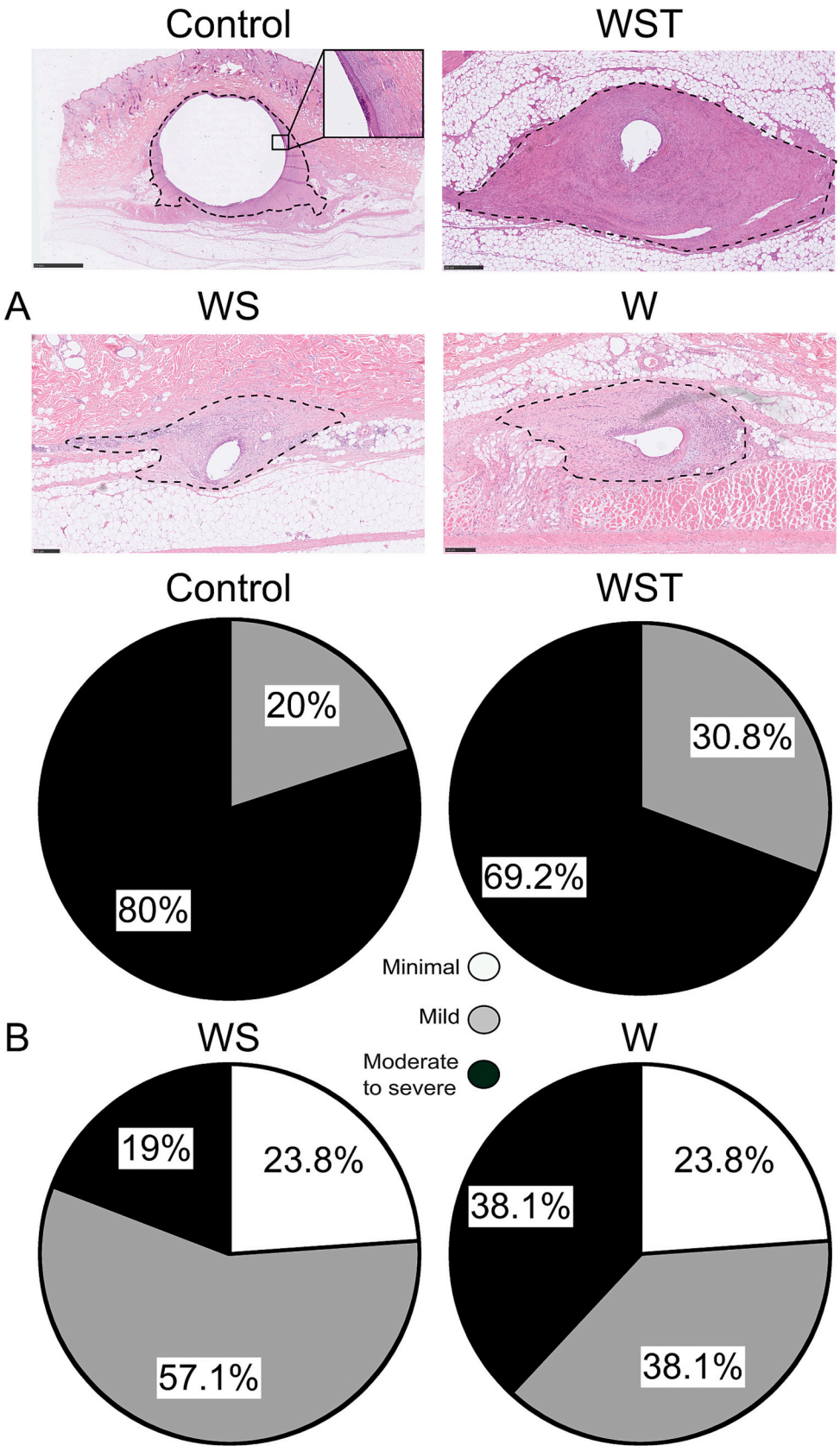

Fig. 3. Histopathological observations of tissue reactivity around transdermal wires. A) Representative H&E sections for the *Control* (Scale bar: 2.5 mm), WST (Scale bar: 500 μm), WS and W (Scale bar: 250 μm) implants. The inset of the H&E section for the *Control* implant focuses on the epidermal downgrowth detected at the periphery of the implantation tunnel. The truncated lines trace the boundaries of the fibrotic zone around implantation tunnels. B) The highest percentage of tissues around the *Control* implant demonstrated moderate to severe inflammatory reaction. W and WS have more tissues with minimal and mild reaction compared to the *Control* implant and WST wires. Data presented as percentage of tissues in each category of inflammatory response (i.e., minimal, mild, and moderate to severe).

Table 1
Score system of tissue reactivity around implants.

Score	Tissue reaction
1	Minimal inflammation & fibrosis, absent/ill-defined cellular channel lining
2	Mild fibrosis and inflammation; non-epidermal lining
3	Like 2 but with few multinucleated giant cells
4	Moderate to severe inflammation/fibrosis, non-epidermal lining
5	Like 4 but with multinucleated giant cells
6	Moderate to severe inflammation/fibrosis with epidermal lining

match the cross-sectional conductive area of the *Control* implant, we also plotted the pull-off force per patch that would be needed for the group removal of all wires from each implant condition (Fig. 5D). It was found that the force for the removal of the W (~ 17 ± 4 N) and WS (13.5 ± 2.8 N) patches was higher than the corresponding of either the *Control* implant (~8.8 ± 0.8 N) or the WST (~7.6 ± 2.3 N) patch. Thus, the wire configurations W and WS appear to enable more stable mechanical interactions with the surrounding tissue than the *Control* implant.

The strength of mechanical integration is also dependent on the tissue composition close to the implant. For instance, the transdermal implantation of sutures is frequently characterized by epidermal downgrowth in the subcutaneous tunnel, which subsequently influences the magnitude of the expended force for the removal of sutures from the skin [56,110]. Moreover, deep epidermal growth is indicative of an interfacial path which is accessible to biofilm formation and bacterial migration in the subcutaneous tissues [40,67,112]. We observed epidermal lining in the implantation tunnel for a higher percentage of tissues around the *Control* implant (30 %, in 3 of 4 animals) and the WST (26 %, in 4 of 4 animals) wires, but for limited cases around the W (9 %, in 2 of 4 animals) and WS (10 %, in 1 of 4 animals) wires. Importantly, epidermal lining was restricted to the dermal regions of the implantation tunnel in all of the three experimental groups (i.e., W, WS, WST), with presence only in the subcutaneous tissue for a few cases of the *Control* implant. Representative images of the epidermal lining were obtained by tracking the expression of an epithelial-specific protein marker (i.e., cytokeratin) (Fig. 5E).

Furthermore, epidermal downgrowth engages into dynamic interactions with the cellular and protein components of the fibrotic tissue [113] to collectively orchestrate the progression of FBRs around percutaneous implants [39,114]. Here, Van Gieson's stain was used to analyze the maturity and density of collagen organization as a marker of fibrosis (Table 2) but also the stage of wound healing around implants [91,115]. Following the analysis of representative tissue slices (Supplemental Table T5), the small wires (W and WS) were found surrounded by immature fibrotic tissues (W: 1, WS: 1.2) of low collagen density (W: 1.7, WS: 1.4), Fig. 5F. On the contrary, the fibrotic tissues appeared increasingly mature (WST: 1.4, *Control*: 2) with densely organized collagen fibers (WST: 1.8, *Control*: 2) around the larger implants (WST and *Control*).

3. Discussion

The high demand for advanced therapeutic protocols against the terminal stage of heart failure is on the rise [116,117]. Together with limitations on available donor organs, new protocols to combat frequent complications in mechanical circulatory devices shall expand the use of VADs for the purpose of destination therapy. Lifelong VAD therapies must consider - among other shortcomings – the risks of percutaneous drivelines functioning through chronic wounds of the skin [64,65]. The surgical scheme of percutaneous implantation contributes to DLI which is the most frequent cause of late mortality in VAD implantation [35,118]. Similar complications are met in a broad class of percutaneous devices with loose implant-skin connections such as central catheters [119,120], bionic limbs [121], and neurostimulators [122]. Several attempts to produce fully implantable VADs are pending significant improvements to achieve reliable wireless power transfer [6–8]. Thus, alternative strategies merging new concepts of implant design and biomaterials must be rapidly evolved to eliminate DLIs [2].

In this context, several biophysical parameters of the VAD drivelines shall be rationally optimized to simultaneously direct adaptive integration with skin while satisfying the technical specifications for the therapeutic function of VADs. On the latter, we chose different configurations of small wires with a summed cross-sectional conductive area to equal that of the VAD drivelines. This set-up examined whether several dividends create more stable connections and minimize skin injury compared to the single conduit of VAD drivelines. Our results showed that certain test configurations of thin wires (W and WS) induce milder tissue reactions in their close circumference compared to the commercial HM-III driveline (*Control*). We have schematically summarized the relevant findings in Fig. 6. At the same time, we applied modular protocols of silicone modification to control the chemistry and micron-scale topography at the surface of wires, which are known to ameliorate FBRs and wound healing responses [49,123].

Early on after implantation, biomaterials and medical devices distort the innate inflammatory signals [124], stirring chronic deposition of fibrotic tissue to the surface of the implants [89,124,125]. By investigating how the biophysical properties of transdermal wires influence the fate of chronic skin wounds, we showed that the diameter of implants is the determining factor for stable skin integration. That was confirmed by a series of complementary results showcasing the inflammatory and reactive fibrous responses around the large *Control* (D = 6.5 mm) implants (Fig. 2-5). Despite the high percentage of severe tissue reactions around the WST (D ~ 0.4 mm) wires (Fig. 3), the latter caused milder macroscopic symptoms (Fig. 2) and enabled stronger mechanical interactions with skin (Fig. 5C) than the *Control* implants. Our findings suggest that the size of WST wires (D~ 0.4 mm) may be competing the protective effects of breath topography against fibrosis [46,49]. The role of size as a biophysical driver of FBRs is supported by previous studies, where the increasing size of implants accentuated FBRs and pro-fibrotic responses [58,60,69]. A similar mechanism can explain the comparable inflammatory reactions against W (polyurethane coated) and WS (silicone coated) wires, despite the anti-fibrotic effects of protective polyurethane surfaces on subcutaneous implants [126–128].

In many cases, the accumulation of fibrous tissue on implanted devices raises a barrier to immune surveillance, enacting a breach for bacterial infection [23,129]. The risk of infection escalates when mechanical movements destabilize the implant junction with the tissue, threatening their successful long-term integration [130,131]. VAD drivelines entail similar challenges when exerting mechanical tension to the inhabiting wounds in effect of regular body movements [132,133]. To this end, we used a pull-off assay to measure the adhesion strength of implanted wires in the skin tissue (Fig. 5A&B). The wire configurations - W, WS, and WST – appeared more stable compared to the *Control* implant which exhibited lower less shear stress for decohesion from the skin tissue (Fig. 5C). A similar remark was delivered by the force spent for the removal of thin wire configurations (W and WS) with equal conductive cross-sectional area to the *Control* implant (Fig. 5D). This differential mechanical response is possibly the effect of enhanced epidermal downgrowth in the implantation tunnel of the *Control* implant (Fig. 5E), which has been previously shown to prevent the tight connection implants with the contacting tissue [27,134–136]. The combined results on epidermal lining and mechanical adhesion underscored the loose connection of the *Control* implant with skin, justifying this way the increased wound secretion recorded in the macroscopic studies (Fig. 2D).

Additional lines of evidence suggest that implant integration depends on the mechanical mismatch relative to the adjacent tissue ([137–139]; [140]). Here, the small diameter of the transdermal wires is adjoined with low flexural stiffness, thus establishing a more compliant interface to the modes of skin deformation than the *Control* implants [141,142]. The important role of skin-compatible mechanical interfaces

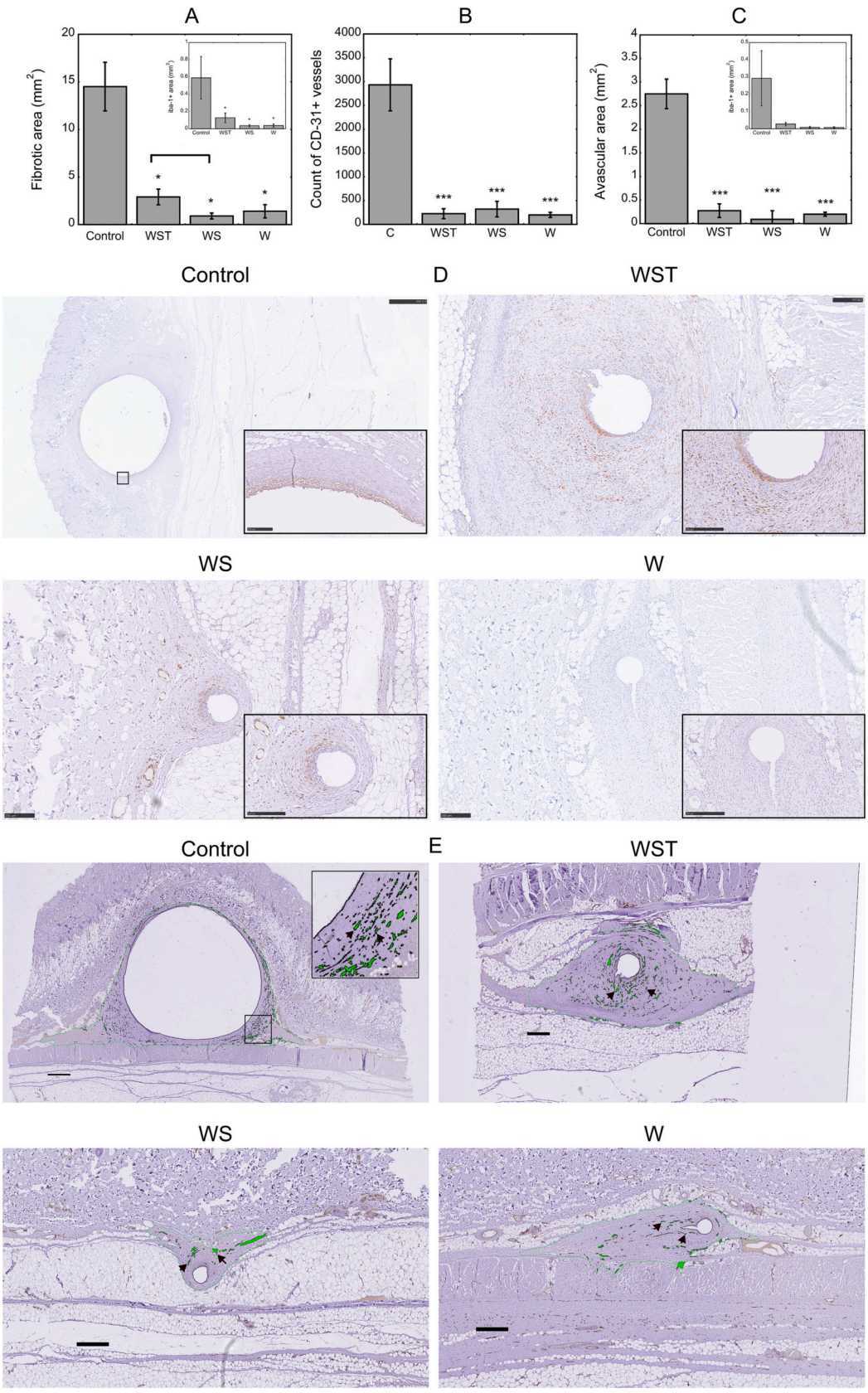

Fig. 4. Quantitative assessment of cellular markers in the fibrotic zone. A) Comparison of the size of the fibrotic area around the implantation tunnels. Inset: Area covered by iba-1 positive macrophages in the fibrotic zone. B) Count of CD31 positive vascular vessels in the fibrotic zone. *P*-values indicated for $P < 0.05$ (*), $P < 0.01$ (**), and $P < 0.001$ (***) relative to the *Control* implant. P-values for the pair comparison of the test wires (WST, WS, W) are indicated above the corresponding bars. C) The size of the avascular zone and its coverage by iba-1 positive cells (inset) close to the implantation tunnels. D) Representative immunohistochemistry images of iba-1 positive macrophages (brown stain). Insets provide a closer view to the iba-1 positive macrophages around implants. E) Representative immunohistochemistry images of CD31 positive vascular vessels (colored in green). The truncated green lines mark the boundaries of the examined fibrotic region in the CD31 stained images. Scale bars: *Control* (2.5 mm), WST, WS and W (250 μm).

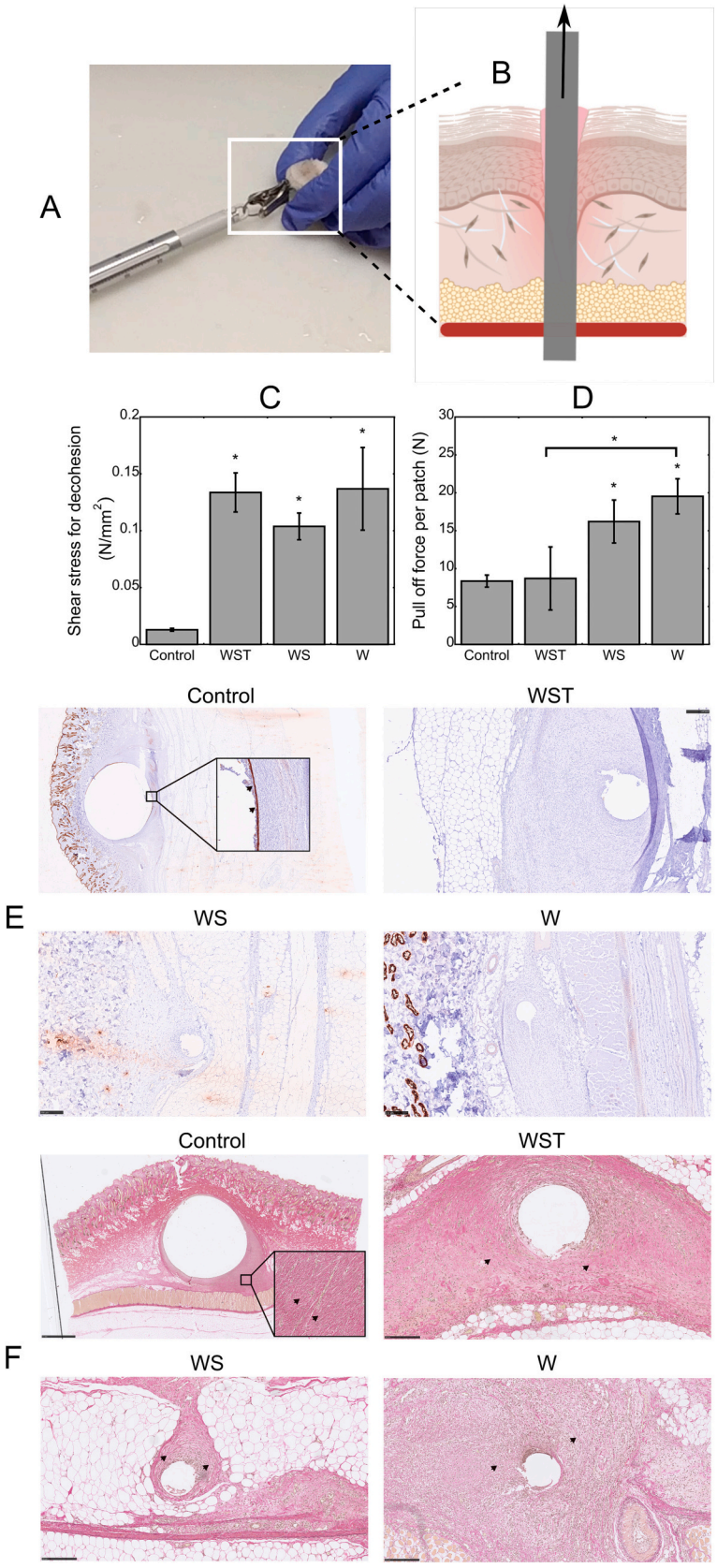

Fig. 5. Mechanical and biological integration of transdermal wires. A & B) Demonstration of the pull-off force assay for the quantitative evaluation of mechanical adhesion at the skin-implant interface. C) Shear stress for the decohesion of implants from the tissue. D) The pull-off force per patch needed for the group removal of implanted wires. *P*-values indicated for $P < 0.05$ (*), $P < 0.01$ (**), and $P < 0.001$ (***) relative to the *Control* implant. P-values for the pair comparison of the test wires (WST, WS, W) are indicated above the corresponding bars. E) Representative immunohistochemistry images stained with cytokeratin for the assessment of epidermal downgrowth. The positively stained epithelial cells (dark brown) at the inset of the *Control* implant highlights the presence of epidermal downgrowth. On the contrary, epidermal downgrowth is absent in the lower dermal levels around the test wires (WST, WS, W). F) Van Gieson stain reveals a mature and dense collagen network around the *Control* implant (inset). Scale bars: *Control* (2.5 mm), WST, WS and W (250 μm). Black arrows point to representative regions of collagen organization for each implant condition.

Table 2
Semi-quantitative score of collagen organization in the fibrotic tissue.

Score	Tissue maturity
1	Immature
2	Mature
	Collagen density
1	Low
2	Moderate
3	High

was also implied by the lower incidence of DLIs in VAD drivelines with low bending force [36,59]. Hence, the increased mechanical mismatch between the *Control* implants and the skin suggests a distinct biophysical signal that may be responsible for the mature collagen network formed adjacent to the epidermal line (Fig. 5E&F), a characteristic which is previously linked to incomplete wound healing around percutaneous implants [134]. Although vascularization has a controversial role to the level of inflammatory reactions [90,95,97,98], the enhanced infiltration of macrophages in the avascular regions (Supplemental Fig.F4D&E) revealed a biphasic correlation between vascularization and inflammatory reactions, which is dictated by the distance from the surface of the implants. Interestingly, vascularization was strongly enhanced in the fibrotic zone of the *Control* implants (Fig. 4B), without similar effects noticed in response to the chemical and topographical cues presented on the surface of the test wires (W, WS and WST). According to the findings of the histological and macroscopic studies, neither the test nor the *Control* implants demonstrated signs of infection. The latter result does not exclude the presence of bacterial colonization at the wire-implant interface, indicating the need for additional investigations related to the incidence of DLIs.

4. Conclusions

The elimination of DLIs will reduce post-surgical complications and mortality, improving the therapeutic impact of VADs. This goal entails the development of new transdermal implants that become well-integrated with the human skin. To this end, we examined the role of diameter, surface topography and chemistry on the integration of transdermal wires with the skin tissue in vivo. We combined macroscopic and histological observations with a pull-off force assay to simultaneously assess tissue reactivity and mechanical adhesion. The large *Control* implants caused severe inflammatory and reactive fibrous responses with epidermal lining in the implantation tunnel. These local tissue effects were found to impede the dermal integration of the *Control* implants, which is a critical prerequisite for the restoration of the barrier function in the wounded skin. We also demonstrated the enhanced mechanical integration of small transdermal wires with skin, which was further supported by the healthy-like matrix organization in the respective fibrotic zones. This work revealed unique mechanical and biological facets related to the implantation of transdermal wires in vivo. The absence of implant-associated infection in this study offers a useful insight into the biological processes evolving before the clinical diagnosis of DLI. Future studies shall concurrently investigate the electrical function, the skin injury, and the incidence of infection related to the implantation of transdermal wires for longer postsurgical periods ($t > 1$ month), including the challenge of superficial contamination with DLI-related bacterial strains. Altogether, this study delivers a novel strategy on the design of new transdermal implants with the potential to facilitate power and signal transmission through the human skin for various therapeutic applications.

5. Materials and methods

5.1 Surface modification of conductive wires with selected topography.

We created enameled copper wires with RTV silicone (RTV4420 A + B at a 1:1 ratio, supplied by Elkem silicone, France) following a method of free-form topography demonstrated in previous protocols [2,70]. Enameled copper wires (Product code: 155–17, 230 supplied by Distrelec) of known length (~6 cm) and diameter (D = 0.2 mm) are immersed in a mixture of degassed RTV silicone and immediately subject to spin coating for selected period (120 s) and speed (700 rpm). The RTV coated wires are subject to periodic rotation until complete solidification into a flat silicon layer around the wires. Throughout this study, these silicone coated wires are denominated as WS while the starting enamel copper wires (polyurethane modified) as W.

To engrave surface topography with breath features, spin-coated wires (D = 0.4 mm. Product code: 155–17,438 supplied by Distrelec) with semi-cured RTV are first transferred into a freezer (−20 °C for 6 min) and then incubated into a humidity chamber (32 °C and relative humidity 100 % for 20 min). Certain features of the transferred topography, such as diameter and depth of breath features in WST wires were captured and quantified by specialized confocal microscopy and MATLAB code, respectively [70,143].

5.1. Experimental animals

The animals used in this study were female sheep (Species: *Ovis aries*, Strain: Blanche du Massif Central) acclimated and housed in-group conditions according to European requirements (Directive EU/2010/63). The study was performed at one of the accredited (AAALAC) facilities of NAMSA (Lyon, France), applying details related to personnel training, animal anesthesia, and veterinary care according to

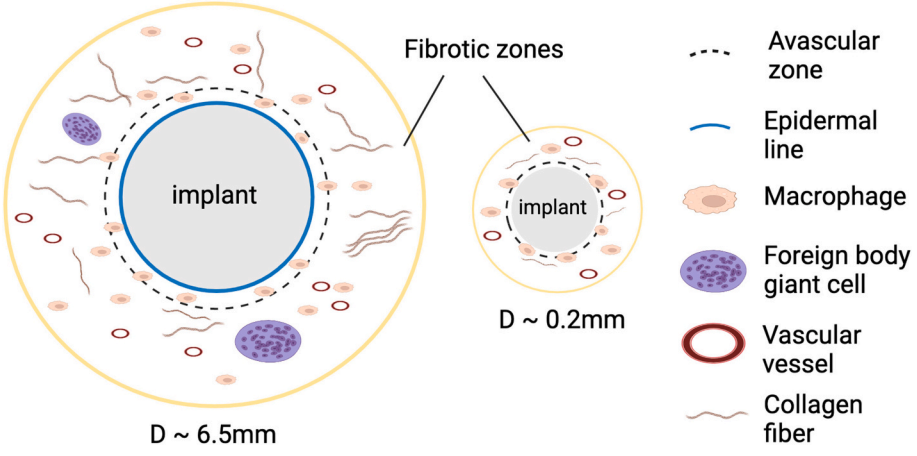

Fig. 6. Schematic summary of overall findings. The diameter of transdermal implants strongly mediated the extend of fibrosis. The *Control* implant (HM-III drivelines, D ~ 6.5 mm) yielded larger fibrotic and avascular zones than the small transdermal wires (D ~ 0.2 mm). Macrophage infiltrates and vascular vessels were detected in the fibrotic zone independent of implant size, while foreign body giant cells were mostly identified around HM-III drivelines. The fibrotic zone of larger implants featured the formation of matured tissues with dense collagen organization. Epidermal lining in the subcutaneous tissue was only detected around HM-III drivelines, impeding their stable mechanical adhesion with skin. The characteristic features of the schematic do not correspond to the physiological length scale of the implant-skin interface. This illustration was created with the scientific software of BioRender.

international standards approved by the ethical committee of NAMSA and authorized by the French Ministry of Education, Higher Education and Research as requested by the ARRIVE guidelines.

5.2. Design of animal trials

This study used four sites on the flank of each animal (2 sites per side) to minimize the final number of animals to four ($n = 4$). Each animal received one control article (C: HM III driveline, D = 6.5 mm, Abbott), a configuration of 12 enameled wires with an individual diameter of 0.2 mm (W), a configuration of 12 silicone coated wires (WS), and a configuration of 3 wires coated with silicone and topographical details of breath features (WST) as described above. As requested by the ISO 10993 standard, Part 6 (2016), the test articles were compared to a commercial control article presenting with similar physical characteristics and clinical intended use. The study was completed in four consecutive stages: animal acclimatization at the facility, implantation of the different configurations, macroscopic observation for four weeks, and study termination followed by tissue collection and histopathological evaluation. Macroscopic observations presented were collected in the first 2 weeks of the study before wool growth obstructs visibility of the wounds.

5.2.1. Housing, husbandry, and environment of the animal study

The animals were housed in-group at arrival until the end of the study according to the European requirements (Directive EU/2010/63) at the animal facility of NAMSA. The animals were kept under laboratory conditions with daily recording of the room temperature (15 - 24 ^{o}C) and relative humidity. The light cycle was controlled using an automatic timer (12 h of light, 12 h of dark). Within 2 weeks prior to surgery, the animals were trained to body suits and jackets, both required to protect the sites after implantation and until the end of the study [51].

5.2.2. Pre-operative procedure

The sheep were shaved without anesthesia by means of clippers and a depilatory cream (Vichy), six (2 animals) and seven (2 animals) days prior to the surgery. Two days prior to the surgery (D-2), the skin of the sheep was cleaned with povidone soap (Medi Scrub Vétédine, Rovers) without anesthesia. The body suits were put on the sheep to protect the skin, while shaving was renewed using clippers and a depilatory cream (Vichy). One day prior to surgery (D-1), the sheep were weighed and subjected to fasting before surgery. The day of surgery (D0), antibiotics (amoxicillin, Clamoxyl Suspension, Zoetis) were administered per-operatively 1 h and 30 min to 6 h and 30 min before pre-medication. Pre-medication was performed by intravenous injection of an analgesic mixture of diazepam (Diazepam® TVM, Laboratoire TVM) and butorphanol (Torphasol®, Axience). Anesthesia was induced by intravenous injection of propofol (Propovet®, Zoetis). The sheep were intubated, mechanically ventilated and placed on isoflurane inhalant anesthetic (IsoFlo®, Zoetis France) for continued general anesthesia. An intravenous infusion with an electrolyte solution (Ringer lactate, Baxter) was performed during surgery. A neutral ophthalmic ointment (Ocrygel®, TVM) was applied to both eyes to protect the corneas from drying and was re-applied as needed. The sheeps were placed in the prone position on a warmed pad. A rectal temperature probe and a rumen tube was placed during surgery. Electrocardiogram (ECG), peripheral non-invasive arterial blood pressure and oxygen saturation were monitored. The surgical areas were disinfected with chlorhexidine soap (Medi Scrub Chlorexidine, Rovers Medical) and chlorhexidine spray (Cooper). When any abnormality was detected (signs of awakening, reaction to palpation, movements of the animal, palpetal reflexes, stiffness, tremors), additional anesthetic agent were administered.

5.2.3. Surgical preparation and articles implantation

Test and control articles were provided aseptically prepared, and they remained immersed in 70 % isopropyl alcohol for 44 to 109 min prior to implantation. The surgery was performed by a NAMSA qualified and trained operator using standard aseptic techniques. The surgical area localized on the flank was around 10 cm at distance from the spine and approximately 10 cm at distance from the front and hind legs. For each test article, small puncture was created through the skin parallel to the spinal column with intravenous catheter (14G, Vasofix® Certo, B Braun) to have approximately 2.5 cm of skin between the entry and the exit points. The catheters were removed after the test articles were passed through their lumen. For both test articles "W" and "WS", the 12 wires were implanted in two columns (6 wires/column) separated by around 5 cm. For test article "WST", three wires were implanted in one column (Fig. 2). The distance between each implanted wire of a same column was approximately 1 cm. For the *Control* implant, one subcutaneous tunnel was created by incising the skin at two points using a biopsy punch of 5 mm diameter and subsequent atraumatic preparation of a tunnel in the subcutaneous tissue with surgical scissors, a solution commonly applied for the implantation of VAD drivelines [64,65]. The tunnel measured approximately 2.5 cm. Implantation of the control article was performed by channelling through the subcutaneous tunnel. The two extra-cutaneous parts of the test and control articles were stabilized on the skin with non-absorbable sutures (Prolene™ 2–0 for the control article and Prolene™ 3–0 for the test articles) at distance from the entry/exit points of each implanted article. For the *Control* implant, the stitches were doubled at both edges with one additional stitch applied in either entry or exist point to reinforce the fixture. During implantation, traces of blood were gently wiped and removed using lukewarm sterile saline solution (NaCl 0.9 %, Lavoisier).

5.2.4. Postsurgical treatment, observations, and terminal procedure

After surgery, the wounds were sprayed with chlorhexidine solution (Chlorexidine Spray, Cooper). Sterile non-woven dry gauzes and adhesive dressing (Urgoderm, Urgo) were applied to protect the implanted sites. Next, the protective body suits and the jackets were put on and the animals were moved to a recovery area, monitoring the recovery from anesthesia until sternal recumbency was achieved. After recovery, the animals were returned to their cages and observed for general health.

Animals were observed daily for general health and to detect mortality and morbidity. In addition, a detailed clinical examination of the animals was conducted upon arrival of the animal, prior to conduct the surgery and 15 days after the surgery. The integrity of the body suits and the jackets was monitored every day. They were changed as necessary when soiled or damaged. Precautions were taken to avoid any contamination of the wounds. The dressing integrity was monitored 3 times a week from the day of the surgery up to the 18th day post-surgery and no further due to the rapid growth of the wool.

During the first three days after implantation and once a day, the protective body suits and jackets were removed and the area on the dressing of the implanted sites were macroscopically examined. It is noteworthy to mention that the wound was not scored over the first 3 days. The following day (D4 after implantation), the protective body suits, the jackets as well as the dressing were removed to conduct macroscopic observations of the implants according to an established score method (Supplemental T2A). These observations were then conducted three times a week without anesthesia until it was no longer possible due to wool growth, which was 18 days after the implantation. Upon the observations, the implanted sites were examined, with particular attention to the entry and exit points of the articles. The dressing was changed (sterile non-woven dry gauzes and adhesive dressing) after each observation. At each observation point and for each site, 1) the state of the wound was scored for redness, secretion, heat, and swelling. For the all the tested implants, 1) the state of the wound was scored for the whole site. 2) the position of the article was noted (right, left, top, bottom), 3) gross changes or any other adverse changes at the implantation sites were noted, 4) macroscopic pictures of the sites were taken to track the progression of the surgical wounds from D4 to

termination. Over the first 3 days, pictures were taken only upon signs of secretion.

On week 4, the animals were weighed and then euthanized by an intravenous injection of a lethal solution (Doléthal®, Vetoquinol). The implantation sites were macroscopically examined and pictures of the areas of interest were captured. The implantation sites were harvested, fixed, and stored in 10 % Neutral Buffered Formalin (NBF, VWR) for further histopathologic analysis.

5.3. Histological preparation and analysis

Tissue preparation, handling, and analysis were performed blindly, without knowledge of the characteristic properties of the implants. For the *Control* implant, only one driveline with the associated tissue was available per location. For the wires (W, WS, WST), the tissues and the subcutaneous wires were vertically cut half-way between the entrance and the exit sites of the implanted wires. Then, the driveline and the cut wire were removed from the formalin-fixed tissues before the latter become dehydrated through an ethanol series and embedded into paraffin blocks [144,145]. The embedded tissues were trimmed at three different tissue sections, corresponding to the entry site, the exit site, and the deepest point of the implantation channel. For the surgical sites with W, WS and WST wires, the skin tissue in contact with three different wires (wire 1 to 3) per location was further processed for histology (total: 120 sections).

The tissue was routinely processed for histological examination by staining with hematoxylin and eosin (HE), performed by a board-certified veterinary pathologist (Simone de Brot). The HE stained tissue slides were digitalized (Slide Scanner HAMAMATSU Nanozoomer S360) and then assessed for the presence of implant-associated fibrotic and inflammatory tissue changes. The implantation channels were analyzed for defined qualitative and quantitative parameters, as indicated in the results. Quantitative digital histology analysis was performed using Visiopharm software version 2022.07 (Horsholm, Denmark). Regions of interest were manually defined. Tissue vascularization (CD-31 staining) and macrophage quantification (Iba-1 staining) was performed in an automated manner (threshold classification).

When evaluating the histology slide, the sections were classified as cross (C), longitudinal (L) (with channel lumen) and tangential (T) (without channel lumen). Tangential sections were not further analyzed. Where relevant, cases with multiple sections on the histology slide were assessed separately. The fibrotic and the avascular area were quantified by tracking the remodeled dermal tissue around the implantation tunnel and the presence of CD-31 positive vessels, respectively. In addition to the grading score of Table 1, the histopathological features were also scored in a blind fashion according to a semi-quantitative scoring system in compliance with the Annex E of International Standards Organization (ISO) 10,993–6-2016, which evaluates the extend of fibrosis, the nature of inflammatory reaction, the degeneration/necrosis, and the level of vascularization among others (Supplemental Table T3B).

Immunohistochemical evaluation was also performed to detect ionized calcium binding adaptor molecule 1 (Iba-1/macrophages), CD-31 (endothelial cells), and PCK (Epidermal cells). For Iba1, CD20 and PCK antibodies, Dako autostainer (Dako, Glostrup, Denmark) system was used. Briefly, antigen retrieval was performed in all the antibodies using citrate buffer (pH 6) at 98 °C for 20 min or EDTA buffer (pH 9) at 98° for 20 min and CC1 buffer (pH 8.4). Subsequently, endogenous peroxidase activity was quenched with hydrogen peroxidase for 10 min. Primary antibodies were incubated for 1 h followed by secondary antibody application. Rabbit pAb (019–19,741, 1:1000 dilution, supplied by Wako) was used in combination with Envision rabbit (Dako K4003) for detection of iba-1 expression. PECAM-1 sc1506R (1:1000 dilution, supplied by Santa Cruz) was used in combination with Envision rabbit (Dako K4003) for detection of CD-31 expression. Similarly, Cytokeratin PCK 26 (NB120–6401, Novus biologicals) was used in combination with Envision rabbit (Dako K4003) for detection of cytokeratin expression. Finally, sections were counterstained with hematoxylin for 2 s and mounted. Lymph node served as positive control for Iba1 antibodies.

5.4. Mechanical characterization of wire integration into the skin

We assessed the force required to pull-off the implanted wires by means of an ultra-light spring scale (PESOLA, item no. 10500: capacity 500 h, gradient 5 g). In all cases, the assay was performed on tissue extracts that had been stored in formalin at the end of the animal trial (day 28). The tissues and the subcutaneous wires were vertically cut half-way between the entrance and the exit sites of the implanted wires. Note that the *Control* implants and their surrounding tissue were not subject to the latter cutting step. The wire edge pending outside the skin was clamped to the spring scale and exposed to continuous pulling. The force (g) measured at the point of decohesion of the implant from the tissue was recorded and used for the calculation of shear stress and pull-off force. It is worth noting that the length of implants in contact with skin measured immediately after their removal was 3.5 ± 0.1 cm for the *Control,* 0.9 ± 0.2 *cm for the WST,* 1 ± 0.04 *cm for the WS, and* 0.9 ± 0.07 *cm for the W implants.* For the calculation of the pull-off force per patch, we multiplied the mean pull-off force per wire condition (F_{mean}) with the number of wires in each configuration (W: 12, WS: 12, WST:3) and the sum of entry and exit sites per wire (n=2) in accordance with the surgical scheme and the vertical cut of wires before pulling them off of the skin tissue. This is, the pull of force per patch for W is $F=2x12xF_{mean}(W)$, for WS is $F=2x12xF_{mean}(WS)$, and for WST is $F=2x3xF_{mean}(WST)$.

5.5. Statistical analysis

We performed ANOVA with a Student's-Newman-Keuls post hoc test for the statistical comparison of the measured parameters (i.e., area of fibrotic tissue, area of macrophage cells, absolute count of vessels, shear stress for decohesion, pull-off force per patch, redness, and secretion) measured for the four conditions of percutaneous implants (W, WS, WST, *Control*). The error bars depict the standard error of the mean.

Declaration of competing interest

The authors declare the following financial interests/personal relationships which may be considered as potential competing interests: Andreas Kourouklis, Xi Wu, Aldo Ferrari, and Edoardo Mazza have filed a patent (EP20208958.7) for protection of the technology described in the manuscript. All other authors have no interest to declare.

Data availability

The raw/processed data required to reproduce these findings cannot be shared at this time due to technical or time limitations.

Appendix A. Supplementary data

Supplementary data to this article can be found online at https://doi.org/10.1016/j.bioadv.2023.213568.

References

[1] R.J.H. Miller, J.J. Teuteberg, S.A. Hunt, Innovations in ventricular assist devices for end-stage heart failure, Annu. Rev. Med. 70 (2019) 33–44, https://doi.org/10.1146/annurev-med-041217-011015.
[2] A.P. Kourouklis, et al., Systems of conductive skin for power transfer in clinical applications, Eur. Biophys. J. (2021), https://doi.org/10.1007/s00249-021-01568-8.
[3] L. Miller, E. Birks, M. Guglin, H. Lamba, O.H. Frazier, Use of ventricular assist devices and heart transplantation for advanced heart failure, Circ. Res. 124 (2019) 1658–1678, https://doi.org/10.1161/CIRCRESAHA.119.313574.
[4] T. Campi, S. Cruciani, F. Maradei, A. Montalto, F. Musumeci, M. Feliziani, Centralized High Power Supply System for Implanted Medical Devices Using Wireless Power Transfer Technology IEEE Transactions on Medical Robotics and Bionics 3, 2021, pp. 992–1001, https://doi.org/10.1109/TMRB.2021.3123404.

[5] O. Knecht, R. Bosshard, J.W. Kolar, High-efficiency transcutaneous energy transfer for implantable mechanical heart support systems IEEE transactions on power, Electronics 30 (2015) 6221–6236, https://doi.org/10.1109/Tpel.2015.2396194.

[6] B. Letzen, J. Park, Z. Tuzun, P. Bonde, Design and development of a miniaturized percutaneously deployable wireless left ventricular assist device: early prototypes and feasibility testing, ASAIO J. 64 (2018) 147–153, https://doi.org/10.1097/Mat.0000000000000669.

[7] Y. Pya, et al., First human use of a wireless coplanar energy transfer coupled with a continuous-flow left ventricular assist device, J. Heart Lung Transplant. 38 (2019) 339–343, https://doi.org/10.1016/j.healun.2019.01.1316.

[8] B.H. Waters, et al., Electrical power to run ventricular assist devices using the free-range resonant electrical energy delivery system, J. Heart Lung Transplant. 37 (2018) 1467–1474, https://doi.org/10.1016/j.healun.2018.08.007.

[9] P. Angleitner, et al., Blood stream infection and outcomes in recipients of a left ventricular assist device, Eur. J. Cardiothorac. Surg. 58 (2020) 907–914, https://doi.org/10.1093/ejcts/ezaa153.

[10] H. Copeland, D. Baran, A persistent problem—the dreaded LVAD driveline infection, J. Card. Surg. 37 (2022) 105–106, https://doi.org/10.1111/jocs.16075.

[11] G.A. Hernandez, J.D. Nunez Breton, S.V. Chaparro, Driveline infection in ventricular assist devices and its implication in the present era of destination therapy open, J. Cardiovasc. Surg. (2017), https://doi.org/10.1177/1179065217714216.

[12] J.K. Kirklin, et al., Eighth annual INTERMACS report: special focus on framing the impact of adverse events, J. Heart Lung Transplant. 36 (2017) 1080–1086, https://doi.org/10.1016/j.healun.2017.07.005.

[13] Pavlovic NV, Randell T, Madeira T, Hsu S, Zinoviev R, Abshire M (2019) Risk of left ventricular assist device driveline infection: a systematic literature review. doi:https://doi.org/10.1016/j.hrtlng.2018.11.002.

[14] J.K. Kirklin, et al., American Association for Thoracic Surgery/International Society for Heart and Lung Transplantation guidelines on selected topics in mechanical circulatory support, J. Thorac. Cardiovasc. Surg. 159 (2020) 865–896, https://doi.org/10.1016/j.jtcvs.2019.12.021.

[15] P. Shah, et al., Twelfth interagency registry for mechanically assisted circulatory support report: readmissions after left ventricular assist device, Ann. Thorac. Surg. 113 (2022) 722–737, https://doi.org/10.1016/j.athoracsur.2021.12.011.

[16] S. Agrawal, et al., Thirty-day readmissions after left ventricular assist device implantation in the United States: insights from the Nationwide readmissions database, Circ Heart Fail 11 (2018), e004628, https://doi.org/10.1161/CIRCHEARTFAILURE.117.004628.

[17] Hannan MM et al. (2011) Working formulation for the standardization of definitions of infections in patients using ventricular assist devices vol 30. doi: https://doi.org/10.1016/j.healun.2011.01.717.

[18] W.L. Holman, Microbiology of infection in mechanical circulatory support, Int. J. Artif. Organs 30 (2007) 764–770, https://doi.org/10.1177/039139880703000904.

[19] I. Kamat, et al., Identifying causative microorganisms in left ventricular assist device infections as a guide for developing bacteriophage therapy, J. Surg. Res. 271 (2022) 73–81, https://doi.org/10.1016/j.jss.2021.10.010.

[20] Y. Qu, Anton Y. Peleg, David McGiffin, Ventricular assist device-specific infections, J. Clin. Med. 10 (2021), https://doi.org/10.3390/jcm10030453.

[21] B.N. Brown, B.D. Ratner, S.B. Goodman, S. Amar, S.F. Badylak, Macrophage polarization: an opportunity for improved outcomes in biomaterials and regenerative medicine, Biomaterials 33 (2012) 3792–3802, https://doi.org/10.1016/j.biomaterials.2012.02.034.

[22] A. Kar, N. Ahamad, M. Dewani, L. Awasthi, R. Patil, R. Banerjee, Wearable and implantable devices for drug delivery: applications and challenges, Biomaterials 283 (2022), 121435, https://doi.org/10.1016/j.biomaterials.2022.121435.

[23] D. Isackson, L.D. McGill, K.N. Bachus, Percutaneous implants with porous titanium dermal barriers: an in vivo evaluation of infection risk, Med. Eng. Phys. 33 (2011) 418–426, https://doi.org/10.1016/j.medengphy.2010.11.007.

[24] J.A. Jansen, Y.G.C.J. Paquay, J.P.C.M. van Der Waerden, Tissue reaction to soft-tissue anchored percutaneous implants in rabbits, J. Biomed. Mater. Res. 28 (1994) 1047–1054, https://doi.org/10.1002/jbm.820280909.

[25] D.R.L. Pawar, S. Jeyapalina, K. Hafer, K.N. Bachus, Influence of negative pressure wound therapy on peri-prosthetic tissue vascularization and inflammation around porous titanium percutaneous devices, Journal of Biomedical Materials Research Part B-Applied Biomaterials 107 (2019) 2091–2101, https://doi.org/10.1002/jbm.b.34302.

[26] B. Chehroudi, D.M. Brunette, Subcutaneous microfabricated surfaces inhibit epithelial recession and promote long-term survival of percutaneous implants, Biomaterials 23 (2002) 229–237, https://doi.org/10.1016/S0142-9612(01)00100-4.

[27] A. Oyane, K. Hyodo, M. Uchida, Y. Sogo, A. Ito, Preliminary in vivo study of apatite and laminin-apatite composite layers on polymeric percutaneous implants, J Biomed Mater Res B Appl Biomater 97 (2011) 96–104, https://doi.org/10.1002/jbm.b.31790.

[28] J. Tillander, K. Hagberg, L. Hagberg, R. Branemark, Osseointegrated titanium implants for limb prostheses attachments: infectious complications, Clin. Orthop. Relat. Res. 468 (2010) 2781–2788, https://doi.org/10.1007/s11999-010-1370-0.

[29] R.A. Underwood, et al., Quantifying the effect of pore size and surface treatment on epidermal incorporation into percutaneously implanted sphere-templated porous biomaterials in mice, Journal of Biomedical Materials Research Part A 98a (2011) 499–508, https://doi.org/10.1002/jbm.a.33125.

[30] A.M. Bernhardt, T. Schlöglhofer, V. Lauenroth, F. Mueller, M. Mueller, A. Schoede, C. Klopsch, Prevention and early treatment of driveline infections in ventricular assist device patients - the DESTINE staging proposal and the first standard of care protocol, J. Crit. Care 56 (2020) 106–112, https://doi.org/10.1016/j.jcrc.2019.12.014.

[31] O. Haddad, A.N. Pham, M. Thomas, M. Ali, B. Sareyyupoglu, M.M. El-Sayed Ahmed, S.M. Pham, Absorbable antibiotic beads as an adjuvant therapy in treating ventricular assist devices driveline infection: a case report, J. Card. Surg. 35 (2020) 2073–2076, https://doi.org/10.1111/jocs.14778.

[32] M. Cikirikcioglu, K. Ponchant, N. Murith, P. Meyer, N. Yilmaz, C. Huber, Treatment of HeartMate III–LVAD driveline infection by negative pressure wound therapy: result of our case series the, Int. J. Artif. Organs 44 (2021) 912–916, https://doi.org/10.1177/03913988211047250.

[33] Z.O. Koken, et al., Driveline exit-site care protocols in patients with left ventricular assist devices: a systematic review, Eur J Cardiothorac Surg. 60 (2021) 506–515, https://doi.org/10.1093/ejcts/ezab195.

[34] S. Kusne, et al., An ISHLT consensus document for prevention and management strategies for mechanical circulatory support infection, J Heart Lung Transplant 36 (2017) 1137–1153, https://doi.org/10.1016/j.healun.2017.06.007.

[35] M. Pieri, et al., Surgical management of driveline infections in patients with left ventricular assist devices, J. Card. Surg. 31 (2016) 765–771, https://doi.org/10.1111/jocs.12860.

[36] T. Imamura, T. Murasawa, H. Kawasaki, K. Kashiwa, O. Kinoshita, K. Nawata, M. Ono, Correlation between driveline features and driveline infection in left ventricular assist device selection, Journal of Artif. Organs 20 (2017) 34–41, https://doi.org/10.1007/s10047-016-0923-8.

[37] E.C.L. Bolle, N. Bartnikowski, P. Haridas, T.J. Parker, J.F. Fraser, S.D. Gregory, T. R. Dargaville, Improving skin integration around long-term percutaneous devices using fibrous scaffolds in a reconstructed human skin equivalent model, J Biomed Mater Res B Appl Biomater 108 (2020) 738–749, https://doi.org/10.1002/jbm.b.34428.

[38] A.S. Cavalcanti, et al., In vivo evaluation of skin integration with ventricular assist device drivelines, The Journal of Heart and Lung Transplantation (2022), https://doi.org/10.1016/j.healun.2022.03.014.

[39] Y. Fukano, et al., Epidermal and dermal integration into sphere-templated porous poly(2-hydroxyethyl methacrylate) implants in mice, Journal of Biomedical Materials Research Part A 94a (2010) 1172–1186, https://doi.org/10.1002/jbm.a.32798.

[40] J. Großhauser, K. Reiter, C. Große-Siestrup, J. Kikhney, U. Kertzscher, K. Affeld, Bionic approach for the prevention of exit-site infections of percutaneous devices, Biomed. Tech. (2015), https://doi.org/10.1515/bmt-2014-0062.

[41] D. Camboni, M. Zerdzitzki, S. Hirt, R. Tandler, M. Weyand, C. Schmid, Reduction of INCOR (R) driveline infection rate with silicone at the driveline exit site, Interact. Cardiovasc. Thorac. Surg. 24 (2017) 222–228, https://doi.org/10.1093/icvts/ivw336.

[42] D. Dean, et al., Reduction in driveline infection rates: results from the HeartMate II multicenter driveline silicone skin Interface (SSI) registry, J. Heart Lung Transplant. 34 (2015) 781–789, https://doi.org/10.1016/j.healun.2014.11.021.

[43] H.J. Busscher, et al., Biomaterial-associated infection: locating the finish line in the race for the surface, Sci. Transl. Med. 4 (2012) 153rv110, https://doi.org/10.1126/scitranslmed.3004528.

[44] R.O. Darouiche, Device-associated infections: a macroproblem that starts with microadherence, Clin. Infect. Dis. 33 (2001) 1567–1572, https://doi.org/10.1086/323130.

[45] S.W. Lee, K.S. Phillips, H. Gu, M. Kazemzadeh-Narbat, D.C. Ren, How microbes read the map: effects of implant topography on bacterial adhesion and biofilm formation, Biomaterials (2021) 268, https://doi.org/10.1016/j.biomaterials.2020.120595.

[46] T. Kawano, Y. Nakamichi, S. Fujinami, K. Nakajima, H. Yabu, M. Shimomura, Mechanical regulation of cellular adhesion onto honeycomb-patterned porous scaffolds by altering the elasticity of material surfaces, Biomacromolecules 14 (2013) 1208–1213, https://doi.org/10.1021/bm400202d.

[47] H. Majd, et al., Novel micropatterns mechanically control fibrotic reactions at the surface of silicone implants, Biomaterials 54 (2015) 136–147, https://doi.org/10.1016/j.biomaterials.2015.03.027.

[48] C. Park, et al., Reduced fibrous capsule formation at nano-engineered silicone surfaces via tantalum ion implantation, Biomaterials Science 7 (2019) 2907–2919, https://doi.org/10.1039/c9bm00427k.

[49] F. Robotti, et al., A micron-scale surface topography design reducing cell adhesion to implanted materials, Sci Rep 8 (2018) 10887, https://doi.org/10.1038/s41598-018-29167-2.

[50] K. Wang, et al., Overcoming foreign-body reaction through nanotopography: biocompatibility and immunoisolation properties of a nanofibrous membrane, Biomaterials 102 (2016) 249–258, https://doi.org/10.1016/j.biomaterials.2016.06.028.

[51] J. Kaemmel, et al., On the function of biosynthesized cellulose as barrier against bacterial colonization of VAD drivelines, Scientific Report 11 (2021) 18776, https://doi.org/10.1038/s41598-021-98220-4.

[52] D. Falconnet, G. Csucs, H.M. Grandin, M. Textor, Surface engineering approaches to micropattern surfaces for cell-based assays, Biomaterials 27 (2006) 3044–3063, https://doi.org/10.1016/j.biomaterials.2005.12.024.

[53] A.P. Quist, S. Oscarsson, Micropatterned surfaces: techniques and applications in cell biology, Expert Opin Drug Discov 5 (2010) 569–581, https://doi.org/10.1517/17460441.2010.489606.

[54] R.A. Merchel, et al., 34 impact of driveline material and size on exit site healing time in left ventricular assist devices, J. Heart Lung Transplant. (2012), https://doi.org/10.1016/j.healun.2012.01.037.

[55] S.P. McCandless, et al., Comparing velour versus silicone interfaces at the driveline exit site of HeartMate II devices: infection rates, histopathology, and ultrastructural aspects, Cardiovasc. Pathol. 24 (2015) 71–75, https://doi.org/10.1016/j.carpath.2014.07.011.

[56] R.G. Bennett, Selection of wound closure materials, J. Am. Acad. Dermatol. 18 (1988) 619–637, https://doi.org/10.1016/S0190-9622(88)70083-3.

[57] N. Lekic, S.D. Dodds, Suture materials, needles, and methods of skin closure: what every hand surgeon should know, The Journal of Hand Surgery 47 (2022) 160–171.e161, https://doi.org/10.1016/j.jhsa.2021.09.019.

[58] J.E. Sanders, S.D. Bale, T. Neumann, Tissue response to microfibers of different polymers: polyester, polyethylene, polylactic acid, and polyurethane, J. Biomed. Mater. Res. 62 (2002) 222–227, https://doi.org/10.1002/jbm.10285.

[59] M. Kranzl, et al., Driveline Features as Risk Factor for Infection in Left Ventricular Assist Devices: Meta-Analysis and Experimental Tests Frontiers in Cardiovascular Medicine, 2021, p. 8, https://doi.org/10.3389/fcvm.2021.784208.

[60] E.J. van Rijssel, R. Brand, C. Admiraal, I. Smit, J.B. Trimbos, Tissue reaction and surgical knots: the effect of suture size, knot configuration, and knot volume, Obstet. Gynecol. 74 (1989) 64–68.

[61] L. Coyle, et al., Treatment of HeartMate II short-to-shield patients with an ungrounded cable: indications and long-term outcomes, ASAIO J. 66 (2020) 381–387, https://doi.org/10.1097/MAT.0000000000001012.

[62] N.D. D'Antonio, et al., Driveline damage and repair in continuous-flow left ventricular assist devices: a systematic review, Artif. Organs 45 (2021) 819–826, https://doi.org/10.1111/aor.13901.

[63] L. Bernardi, R. Hopf, D. Sibilio, A. Ferrari, A.E. Ehret, E. Mazza, On the cyclic deformation behavior, fracture properties and cytotoxicity of silicone-based elastomers for biomedical applications, Polym. Test. 60 (2017) 117–123, https://doi.org/10.1016/j.polymertesting.2017.03.018.

[64] F. Beyersdorf, J. Scheumann, M. Siepe, Implantation of the HeartMate 3—description of the surgical technique operative techniques in thoracic and, Cardiovasc. Surg. 22 (2017) 173–185, https://doi.org/10.1053/j.optechstcvs.2018.04.002.

[65] M.R. Mehra, et al., Primary results of long-term outcomes in the MOMENTUM 3 pivotal trial and continued access protocol study phase: a study of 2200 HeartMate 3 left ventricular assist device implants, Eur. J. Heart Fail. 23 (2021) 1392–1400, https://doi.org/10.1002/ejhf.2211.

[66] J. Curtis, S.D. Steichen, 1.3.2B - silicones, in: W.R. Wagner, S.E. Sakiyama-Elbert, G. Zhang, M.J. Yaszemski (Eds.), Biomaterials Science, Fourth edition, Academic Press, 2020, pp. 109–123, https://doi.org/10.1016/B978-0-12-816137-1.00011-8.

[67] A.F. von Recum, J.B. Park, Permanent percutaneous devices, Crit Rev Bioeng 5 (1981) 37–77.

[68] Johansson F, Wallman L, Fau-Danielsen N, Danielsen N, Fau-Schouenborg J, Schouenborg J, Fau-Kanje M, Kanje M (2009) Porous silicon as a potential electrode material in a nerve repair setting: tissue reactions doi:https://doi.org/10.1016/j.actbio.2009.02.010.

[69] W.K. Ward, E.P. Slobodzian, K.L. Tiekotter, M.D. Wood, The effect of microgeometry, implant thickness and polyurethane chemistry on the foreign body response to subcutaneous implants, Biomaterials 23 (2002) 4185–4192, https://doi.org/10.1016/s0142-9612(02)00160-6.

[70] X. Wu, et al., A free-form patterning method enabling endothelialization under dynamic flow, Biomaterials 273 (2021), 120816, https://doi.org/10.1016/j.biomaterials.2021.120816.

[71] E. McGee Jr., K. Chorpenning, M.C. Brown, E. Breznock, J.A. Larose, D. Tamez, In vivo evaluation of the HeartWare MVAD pump, J. Heart Lung Transplant. 33 (2014) 366–371, https://doi.org/10.1016/j.healun.2013.10.003.

[72] E. Tuzun, K. Roberts, W.E. Cohn, M. Sargin, C.J. Gemmato, B. Radovancevic, O. H. Frazier, In vivo evaluation of the HeartWare centrifugal ventricular assist device, Tex. Heart Inst. J. 34 (2007) 406–411.

[73] M. Weisskopf, M. Kron, T. Giering, T. Walker, N. Cesarovic, The sheep as a pre-clinical model for testing intra-aortic percutaneous mechanical circulatory support devices, Int. J. Artif. Organs 44 (2021) 703–710, https://doi.org/10.1177/03913988211025537.

[74] E.L. Carney, J.B. Clark, J.L. Myers, R. Peterson, R.P. Wilson, W.J. Weiss, Animal model development for the Penn State pediatric ventricular assist device, Artif. Organs 33 (2009) 953–957, https://doi.org/10.1111/j.1525-1594.2009.00896.x.

[75] B. Lukic, et al., Chronic ovine studies demonstrate low thromboembolic risk in the Penn State infant ventricular assist device, ASAIO J. 65 (2019) 371–379, https://doi.org/10.1097/MAT.0000000000000945.

[76] Monreal G, Sherwood LC, Sobieski MA, Giridharan GA, Slaughter MS, Koenig SC (2014) Large animal models for left ventricular assist device research and development. doi:https://doi.org/10.1097/MAT.0000000000000005.

[77] M. Fourneau, C. Canon, D. Van Vlaender, M.J. Collins, S. Fiddyment, Y. Poumay, O. Deparis, Histological study of sheep skin transformation during the recreation of historical parchment manufacture heritage, Science 8 (2020) 78, https://doi.org/10.1186/s40494-020-00421-z.

[78] S. Alharbi, et al., Ovine model of burn wounds grafted with ovine cadaver skin, Burns 48 (2022) 118–131, https://doi.org/10.1016/j.burns.2021.03.007.

[79] R.S. Horne, J.V. Hurley, D.M. Crowe, M. Ritz, B.M. O'Brien, L.I. Arnold, Wound healing in foetal sheep: a histological and electron microscope study, Br. J. Plast. Surg. 45 (1992) 333–344, https://doi.org/10.1016/0007-1226(92)90001-e.

[80] D.L. Traber, R.E. Barrow, D.N. Herndon, 31 - animal models of burn injury, in: W. W. Souba, D.W. Wilmore (Eds.), Surgical Research, Academic Press, San Diego, 2001, pp. 367–377, https://doi.org/10.1016/B978-012655330-7/50033-2.

[81] A. Grada, J. Mervis, V. Falanga, Research techniques made simple: animal models of wound healing, J. Investig. Dermatol. 138 (2018) 2095, https://doi.org/10.1016/j.jid.2018.08.005.

[82] J.A. Jansen, K. de Groot, Guinea pig and rabbit model for the histological evaluation of permanent percutaneous implants, Biomaterials 9 (1988) 268–272, https://doi.org/10.1016/0142-9612(88)90096-8.

[83] D.J. Goldstein, D. Naftel, W. Holman, L. Bellumkonda, S.V. Pamboukian, F. D. Pagani, J. Kirklin, Continuous-flow devices and percutaneous site infections: clinical outcomes, J. Heart Lung Transplant. 31 (2012) 1151–1157, https://doi.org/10.1016/j.healun.2012.05.004.

[84] C.E. Koval, L. Thuita, N. Moazami, E. Blackstone, Evolution and impact of driveline infection in a large cohort of continuous-flow ventricular assist device recipients, J. Heart Lung Transplant. 33 (2014) 1164–1172, https://doi.org/10.1016/j.healun.2014.05.011.

[85] C.N. Lux, Wound healing in animals: a review of physiology and clinical evaluation, Vet. Dermatol. 33 (2022) 91–e27, https://doi.org/10.1111/vde.13032.

[86] H. Sorg, D.J. Tilkorn, S. Hager, J. Hauser, U. Mirastschijski, Skin wound healing: an update on the current knowledge and concepts, Eur. Surg. Res. 58 (2017) 81–94, https://doi.org/10.1159/000454919.

[87] Wound Infection in Clinical Practice (2008) International Wound Journal 5:iii-11 doi:https://doi.org/10.1111/j.1742-481X.2008.00488.x.

[88] X.F. Walboomers, J.A. Jansen, Effect of microtextured surfaces on the performance of percutaneous devices, Journal of Biomedical Materials Research Part A 74A (2005) 381–387, https://doi.org/10.1002/jbm.a.30337.

[89] M.R. Major, V.W. Wong, E.R. Nelson, M.T. Longaker, G.C. Gurtner, The foreign body response: at the interface of surgery and bioengineering, Plast. Reconstr. Surg. 135 (2015) 1489–1498, https://doi.org/10.1097/Prs.0000000000001193.

[90] D.B. Gurevich, K.E. French, J.D. Collin, S.J. Cross, P. Martin, Live imaging the foreign body response in zebrafish reveals how dampening inflammation reduces fibrosis, J. Cell Sci. 133 (2019), https://doi.org/10.1242/jcs.236075 jcs236075.

[91] F. Robotti, et al., Microengineered biosynthesized cellulose as anti-fibrotic in vivo protection for cardiac implantable electronic devices, Biomaterials 229 (2020), 119583, https://doi.org/10.1016/j.biomaterials.2019.119583.

[92] T. Okayasu, J.T. O'Malley, J.B. Nadol Jr., Density of macrophages immunostained with anti-iba1 antibody in the vestibular endorgans after cochlear implantation in the human, Otol Neurotol 40 (2019) e774–e781, https://doi.org/10.1097/MAO.0000000000002313.

[93] M. Ravikumar, et al., The roles of blood-derived macrophages and resident microglia in the neuroinflammatory response to implanted intracortical microelectrodes, Biomaterials 35 (2014) 8049–8064, https://doi.org/10.1016/j.biomaterials.2014.05.084.

[94] G. Valle, et al., Multifaceted understanding of human nerve implants to design optimized electrodes for bioelectronics, Biomaterials 291 (2022), 121874, https://doi.org/10.1016/j.biomaterials.2022.121874.

[95] Detmar M et al. (1998) Increased microvascular density and enhanced leukocyte rolling and adhesion in the skin of VEGF transgenic mice J. Investig. Dermatol. 111:1–6 doi:https://doi.org/10.1046/j.1523-1747.1998.00262.x.

[96] D.B. Gurevich, et al., Live imaging of wound angiogenesis reveals macrophage orchestrated vessel sprouting and regression, EMBO J. 37 (2018), https://doi.org/10.15252/embj.201797786.

[97] R. Tamma, et al., Vascular density and inflammatory infiltrate in primary oral squamous cell carcinoma and after allogeneic hematopoietic stem cell transplantation, Ann. Hematol. 98 (2019) 979–986, https://doi.org/10.1007/s00277-018-3575-3.

[98] A. Tellechea, et al., Increased skin inflammation and blood vessel density in human and experimental diabetes, International Journal of Lower Extremity Wounds 12 (2013) 4–11, https://doi.org/10.1177/1534734612474303.

[99] U. Klueh, D.I. Dorsky, D.L. Kreutzer, Enhancement of implantable glucose sensor function in vivo using gene transfer-induced neovascularization, Biomaterials 26 (2005) 1155–1163, https://doi.org/10.1016/j.biomaterials.2004.04.017.

[100] Morais JM, Papadimitrakopoulos F, Burgess DJ (2010) Biomaterials/tissue interactions: possible solutions to overcome foreign body response AAPS journal 12:188–196 doi:https://doi.org/10.1208/s12248-010-9175-3.

[101] E. Dondossola, B.M. Holzapfel, S. Alexander, S. Filippini, D.W. Hutmacher, P. Friedl, Examination of the foreign body response to biomaterials by nonlinear intravital microscopy, Nat Biomed Eng (2016) 1, https://doi.org/10.1038/s41551-016-0007.

[102] N. Khosravi, A. Maeda, R.S. DaCosta, J.E. Davies, Nanosurfaces modulate the mechanism of peri-implant endosseous healing by regulating neovascular morphogenesis, Communications Biology (2018) 1, https://doi.org/10.1038/s42003-018-0074-y.

[103] J. Chen, et al., Fusion peptide engineered "statically-versatile" titanium implant simultaneously enhancing anti-infection, vascularization and osseointegration, Biomaterials 264 (2021), 120446, https://doi.org/10.1016/j.biomaterials.2020.120446.

[104] W. Chen, et al., An improved osseointegration of metal implants by pitavastatin loaded multilayer films with osteogenic and angiogenic properties, Biomaterials 280 (2022), 121260, https://doi.org/10.1016/j.biomaterials.2021.121260.

[105] Socarras TO, A.C. Vasconcelos, P.P. Campos, N.B. Pereira, J.P. Souza, S. P. Andrade, Foreign body response to subcutaneous implants in diabetic rats, Plos One 9 (2014), e110945, https://doi.org/10.1371/journal.pone.0110945.

[106] G.Q. Zhang, T.H. Ren, X.Q. Zeng, E. Van Der Heide, Influence of surgical suture properties on the tribological interactions with artificial skin by a capstan experiment approach, Friction 5 (2017) 87–98, https://doi.org/10.1007/s40544-017-0140-3.
[107] A. Setiawati, et al., An Accelerated Wound-Healing Surgical Suture Engineered with an Extracellular Matrix Advanced Healthcare Materials vol 10, 2021, https://doi.org/10.1002/adhm.202001686, 2001686.
[108] G.M. Cooney, S.P. Lake, D.M. Thompson, R.M. Castile, D.C. Winter, C.K. Simms, The suture pullout characteristics of human and porcine linea alba, J. Mech. Behav. Biomed. Mater. 68 (2017) 103–114, https://doi.org/10.1016/j.jmbbm.2017.01.033.
[109] G.D. DuRaine, B. Arzi, J.K. Lee, C.A. Lee, D.J. Responte, J.C. Hu, K.A. Athanasiou, Biomechanical evaluation of suture-holding properties of native and tissue-engineered articular cartilage, Biomech. Model. Mechanobiol. 14 (2015) 73–81, https://doi.org/10.1007/s10237-014-0589-1.
[110] P. Kjellin, K. Danielsson, J. Hakansson, K. Agrenius, T. Andersson, P. Stenlund, Biomechanical and histomorphometric evaluation of skin integration on titanium and PEEK implants with different surface treatments, J Mater Sci Mater Med 33 (2022) 68, https://doi.org/10.1007/s10856-022-06687-y.
[111] N. Marsidi, S.A.M. Vermeulen, T. Horeman, R.E. Genders, Measuring forces in suture techniques for wound closure, J. Surg. Res. 255 (2020) 135–143, https://doi.org/10.1016/j.jss.2020.05.033.
[112] M. Sartori, V. Borsari, M. Maglio, S. Brogini, L. Bragonzoni, S. Zaffagnini, M. Fini, Skin adhesion to the percutaneous component of direct bone anchored systems: systematic review on preclinical approaches and biomaterials biomaterials, Science 9 (2021) 7008–7023, https://doi.org/10.1039/d1bm00707f.
[113] P. Fleckman, J.E. Olerud, Models for the histologic study of the skin interface with percutaneous biomaterials, Biomedical Materials (2008) 3, https://doi.org/10.1088/1748-6041/3/3/034006.
[114] Y. Shin, M. Akao, Tissue reactions to various percutaneous materials with different surface properties and structures, Artif. Organs 21 (1997) 995–1001, https://doi.org/10.1111/j.1525-1594.1997.tb00514.x.
[115] V. Kazlouskaya, S. Malhotra, J. Lambe, M.H. Idriss, D. Elston, C. Andres, The utility of elastic Verhoeff-Van Gieson staining in dermatopathology, J. Cutan. Pathol. 40 (2013) 211–225, https://doi.org/10.1111/cup.12036.
[116] Roger VL (2013) Epidemiology of heart failure circulation research 113:646–659 doi:https://doi.org/10.1161/CIRCRESAHA.113.300268.
[117] C.W. Yancy, et al., ACCF/AHA guideline for the management of heart failure: executive summary, Circulation 128 (2013) 1810–1852, https://doi.org/10.1161/CIR.0b013e31829e8807.
[118] T. de By, et al., The European registry for patients with mechanical circulatory support of the European association for cardio-thoracic surgery: third report, Eur J Cardiothorac Surg (2022) 62, https://doi.org/10.1093/ejcts/ezac032.
[119] L.A. Mermel, Prevention of intravascular catheter–related infections, Ann. Intern. Med. 132 (2000) 391–402, https://doi.org/10.7326/0003-4819-132-5-200003070-00009.
[120] N.P. O'Grady, et al., Guidelines for the prevention of intravascular catheter-related infections, Am. J. Infect. Control 39 (2011) S1–S34, https://doi.org/10.1016/j.ajic.2011.01.003.
[121] Bumbasirevic M, Lesic A, Palibrk TD, Milovanovic D, Zoka M, Kravic-Stevovic T, Raspopovic S (2020) The current state of bionic limbs from the surgeon's viewpoint Efort Open Reviews 5:65–72 doi:https://doi.org/10.1302/2058-5241.5.180038.
[122] B.M. Ilfeld, et al., Infection rates of electrical leads used for percutaneous Neurostimulation of the peripheral nervous system, Pain Practice 17 (2017) 753–762, https://doi.org/10.1111/papr.12523.
[123] A. Marmaras, T. Lendenmann, G. Civenni, D. Franco, D. Poulikakos, V. Kurtcuoglu, A. Ferrari, Topography-mediated apical guidance in epidermal wound healing, Soft Matter 8 (2012) 6922–6930, https://doi.org/10.1039/c2sm00030j.
[124] J.M. Anderson, A. Rodriguez, D.T. Chang, Foreign body reaction to biomaterials, Semin. Immunol. 20 (2008) 86–100, https://doi.org/10.1016/j.smim.2007.11.004.
[125] G.R. Goldenberg, A. Barsheshet, J. Bishara, E. Kadmon, A. Omelchencko, B. Strasberg, G. Golovchiner, Effect of fibrotic capsule debridement during generator replacement on cardiac implantable electronic device infection risk, J. Interv. Card. Electrophysiol. 58 (2020) 113–118, https://doi.org/10.1007/s10840-019-00581-4.
[126] F.E. Barone, L. Perry, T. Keller, G.P. Maxwell, The biomechanical and histopathologic effects of surface texturing with silicone and polyurethane in tissue implantation and expansion, Plast. Reconstr. Surg. 90 (1992) 77–86, https://doi.org/10.1097/00006534-199207000-00012.
[127] N. Handel, J. Gutierrez, Long-term safety and efficacy of polyurethane foam-covered breast implants, Aesthet Surg J 26 (2006) 265–274, https://doi.org/10.1016/j.asj.2006.04.001.
[128] S. Manav, M.S. Ayhan, E. Deniz, E. Ozkocer, C. Elmas, M. Yalinay, E. Sahin, Capsular contracture around silicone miniimplants following bacterial contamination: an in vivo comparative experimental study between textured and polyurethane implants, J. Plast. Reconstr. Aesthet. Surg. 73 (2020) 1747–1757, https://doi.org/10.1016/j.bjps.2020.02.049.
[129] B. Jansen, G. Peters, Foreign body associated infection, J. Antimicrob. Chemother. 32 (1993) 69–75, https://doi.org/10.1093/jac/32.suppl_A.69.
[130] B.M. Holt, K.N. Bachus, J.P. Beck, R.D. Bloebaum, S. Jeyapalina, Immediate post-implantation skin immobilization decreases skin regression around percutaneous osseointegrated prosthetic implant systems, J. Biomed. Mater. Res. A 101 (2013) 2075–2082, https://doi.org/10.1002/jbm.a.34510.
[131] J.A. Jansen, J.P. van der Waerden, K. de Groot, Epithelial reaction to percutaneous implant materials: in vitro and in vivo experiments, J. Investig. Surg. 2 (1989) 29–49, https://doi.org/10.3109/08941938909016502.
[132] S.A. Hollander, et al., Obesity and premature loss of mobility in two adolescents with Becker muscular dystrophy after HeartMate II implantation, ASAIO J. 62 (2016), https://doi.org/10.1097/MAT.0000000000000292.
[133] Ogawa M et al. (2018) Internal driveline damage under the costal margin several years after HeartMate II implant: a series of three cases Journal of Artif. Organs 21:359–362 doi:https://doi.org/10.1007/s10047-018-1029-2.
[134] S. Jeyapalina, J.P. Beck, J. Agarwal, K.N. Bachus, A 24-month evaluation of a percutaneous osseointegrated limb-skin interface in an ovine amputation model, J Mater Sci Mater Med 28 (2017) 179, https://doi.org/10.1007/s10856-017-5980-x.
[135] C. Knabe, C. Grosse-Siestrup, U. Gross, Histologic evaluation of a natural permanent percutaneous structure and clinical percutaneous devices, Biomaterials 20 (1999) 503–510, https://doi.org/10.1016/s0142-9612(98)00195-1.
[136] D. Lundgren, R. Axelsson, Soft-tissue-anchored percutaneous device for long-term intracorporeal access, J. Investig. Surg. 2 (1989) 17–27, https://doi.org/10.3109/08941938909016501.
[137] R. Guo, A.R. Merkel, J.A. Sterlin, J.M. Davidson, S.A. Guelcher, Substrate modulus of 3D-printed scaffolds regulates the regenerative response in subcutaneous implants through the macrophage phenotype and Wnt signaling, Biomaterials 73 (2015) 85–95, https://doi.org/10.1016/j.biomaterials.2015.09.005.
[138] M.C. Jordan, S. Boelch, H. Jansen, R.H. Meffert, S. Hoelscher-Doht, Does plastic suture deformation induce gapping after tendon repair? A biomechanical comparison of different suture materials, Journal of Biomechanics 49 (2016) 2607–2612, https://doi.org/10.1016/j.jbiomech.2016.05.023.
[139] D.A. Müller, J.G. Snedeker, D.C. Meyer, Two-month longitudinal study of mechanical properties of absorbable sutures used in orthopedic surgery, J. Orthop. Surg. Res. 11 (2016) 111, https://doi.org/10.1186/s13018-016-0451-5.
[140] Polykandriotis Elias, B.A. Daenicke Jonas, Grüner Jasmin, Dirk W. Schubert, Horch Raymund, Individualized wound closure - mechanical properties of suture, materials, Journal of Personalized Medicine (2022) 12, https://doi.org/10.3390/jpm12071041.
[141] M. Rajabi, et al., Flexible and Stretchable Microneedle Patches with Integrated Rigid Stainless Steel Microneedles for Transdermal Biointerfacing Plos One 11, 2016, e0166330, https://doi.org/10.1371/journal.pone.0166330.
[142] R. Sanders, Torsional elasticity of human skin in vivo, Pflugers Arch. 342 (1973) 255–260, https://doi.org/10.1007/BF00591373.
[143] G.B. Ramirez-Rodriguez, et al., Biomimetic mineralization promotes viability and differentiation of human mesenchymal stem cells in a perfusion bioreactor, Int J Mol Sci (2021) 22, https://doi.org/10.3390/ijms22031447.
[144] C.S. Rutland, et al., Immunohistochemical characterisation of GLUT1, MMP3 and NRF2, Osteosarcoma Front Vet Sci 8 (2021), https://doi.org/10.3389/fvets.2021.704598, 704598.
[145] J. Triscott, et al., PI5P4Kalpha supports prostate cancer metabolism and exposes a survival vulnerability during androgen receptor inhibition, Science Advances 9 (2023), https://doi.org/10.1126/sciadv.ade8641 eade8641.